JOURNAL OF GEOPHYSICAL RESEARCH, VOL. 112, C10022, doi:10.1029/2006JC003839, 2007



# Geometry and dynamics of wave ripples in the nearshore zone of a coarse sandy beach

G. Masselink,[1] M. J. Austin,[2] T. J. O'Hare,[2] and P. E. Russell[2]

Received 25 July 2006; revised 31 May 2007; accepted 21 June 2007; published 24 October 2007.

[1] Extensive measurements of ripple characteristics and dynamics along with associated suspended sediment fluxes and hydrodynamic conditions were made in the shoaling and surf zones of a macrotidal coarse grained beach at Sennen Cove, Cornwall, England (median grain diameter 0.69 mm). Suborbital vortex ripples were observed during the majority of the study period with height ~5 cm and length ~35 cm. The scale and shape of the ripples did not vary significantly as the bed shear stress increased during wave shoaling and breaking. However, ripple migration rates (onshore directed) were strongly dependent on their location relative to the breakpoint, increasing from ~0.1 cm min$^{-1}$ under shoaling waves to 2 cm min$^{-1}$ in the outer surf zone during low-energy conditions. Farther inside the surf zone, ripples persisted but migration rates slowed, probably owing to the presence of the offshore-directed mean flow which impedes landward migration of the ripples. Under low-wave conditions (during which measured sediment fluxes peaked around the outer surf zone and decreased through the saturated surf zone), bed form transport rates under shoaling waves were of the same magnitude as net suspended sediment fluxes but at least an order of magnitude smaller in the outer surf zone. Under high-energy conditions (during which suspended sediment fluxes in the surf zone were offshore directed owing to the presence of the seaward directed mean flow), bed form transport rates were several orders of magnitude smaller than suspended fluxes.

**Citation:** Masselink, G., M. J. Austin, T. J. O'Hare, and P. E. Russell (2007), Geometry and dynamics of wave ripples in the nearshore zone of a coarse sandy beach, *J. Geophys. Res.*, *112*, C10022, doi:10.1029/2006JC003839.

## 1. Introduction

[2] Small-scale bed forms, or ripples, are ubiquitous features in the nearshore zone fronting sandy shorelines and are of fundamental importance to sediment transport processes [cf. *Fredsoe and Deigaard*, 1992; *Nielsen*, 1992]. Firstly, bed forms represent roughness elements for wave- and current-driven flows, controlling to a large degree the structure of the boundary layer [*Grant and Madsen*, 1986]. Secondly, through the generation of near-bed turbulence, bed forms significantly affect the suspended sediment profile, and the magnitude and direction of suspended sediment fluxes [e.g., *Vincent et al.*, 1991]. In addition, bed form migration can provide a means of quantifying the bed load component of the total transport [e.g., *Dyer and Soulsby*, 1988]. Not surprisingly, therefore, considerable attention has been devoted toward obtaining methods for predicting ripple occurrence and geometry from hydrodynamic and sediment parameters [e.g., *Allen*, 1970; *Dingler*, 1974; *Miller and Komar*, 1980; *Nielsen*, 1981; *Grant and Madsen*, 1982; *Wiberg and Harris*, 1994; *Williams et al.*, 2004].

[3] Early investigations, based on laboratory experiments and diver observations, have led to the formulation of various ripple classification schemes. The earliest of these is based on the ratio of ripple height to ripple length, referred to as the ripple steepness $\eta/\lambda$ [*Bagnold*, 1963]. Sharp-crested vortex ripples are characterized by the largest steepness ($\eta/\lambda$ = 0.15) and develop under relatively calm wave energy conditions. Post-vortex ripples have rounded crests and are characterized by smaller steepness values ($\eta/\lambda$ = 0–0.15). Their steepness decreases progressively under increasing wave energy conditions, in the so-called break-off range, and the rippled bed eventually develops into a plane bed when bed stresses exceed a certain threshold [*Nielsen*, 1981]. An alternative ripple scheme is that developed by *Clifton* [1976] and *Clifton and Dingler* [1984], which comprises three different types of wave ripples: (1) orbital ripples with a wave length proportional to the wave orbital diameter; (2) anorbital ripples with a wave length proportional to the sediment size; and (3) suborbital ripples with intermediate wave length. *Wiberg and Harris* [1994] interpreted the different ripple types in terms of the protrusion of the ripples through the wave boundary layer: orbital ripples have heights greater than twice the boundary layer thickness that would occur on a plane bed, whereas anorbital ripples have heights less than one quarter of the boundary layer. Suborbital ripples are transitory. Wave ripples in the nearshore zone mostly fall into the range for suborbital and anorbital ripples, but orbital ripples

[1]School of Geography, University of Plymouth, Plymouth, UK.
[2]School of Earth, Ocean and Environmental Sciences, University of Plymouth, Plymouth, UK.


0148-0227/07/2006JC003839$09.00

may be found in relatively deep water (>10 m) and/or in coarse sediments (>1 mm).

[4] Recent field investigations using a variety of acoustic bed-sensing devices [*Thorne and Hanes*, 2002] have significantly elucidated our understanding of the dynamics of wave ripples. In the shallow nearshore zone (depths up to 5 m), the performance of conventional ripple geometry predictors has been found to range from poor [*Osborne and Vincent*, 1993] to reasonable [*Crawford and Hay*, 2001; *Hanes et al.*, 2001]. One of the difficulties with ripples on natural beaches is the presence of time lags between the development of a particular seabed state and changes in the hydrodynamic forcing, resulting in ripples that are in disequilibrium with the hydrodynamic conditions [*Hay and Bowen*, 1993]. The mismatch between sea bed morphology and hydrodynamic forcing is particularly relevant on beaches where the water level changes rapidly owing to the presence of a large tidal range [*Osborne and Vincent*, 1993]. On such beaches, enhanced sediment resuspension during the falling tide is often observed owing to waves encountering an "oversteepened" bed [*Davidson et al.*, 1993; *Masselink and Pattiaratchi*, 2000]. Recent field studies have also indicated that upper plane bed conditions, which are generally considered to be typical of energetic surf zones [*Clifton*, 1976], are rarely observed. Instead, various 2D or 3D configurations involving large megaripples are commonly present in the surf zone [*Thornton et al.*, 1998; *Hanes et al.*, 2001; *Gallagher*, 2003; *Ngusaru and Hay*, 2004].

[5] Data collected by acoustic bed-sensing devices allow accurate quantification of ripple migration rate and direction. Typical migration rates in shallow (*c.* 5 m) and deep (>10 m) water are $O(1)$ and $O(0.1)$ cm min$^{-1}$ respectively, and ripples can migrate onshore [*Vincent and Osborne*, 1993; *Traykovski et al.*, 1999; *Hanes et al.*, 2001], as well as offshore [*Hay and Bowen*, 1993; *Crawford and Hay*, 2003]. Ripples tend to migrate fastest under energetic wave conditions and positive relationships have been obtained between ripple migration rate and wave orbital velocity $U_m$ [*Traykovski et al.*, 1999], and derivatives of $U_m$, such as the Wave Reynolds Number, Shields Parameter or Mobility Number [*Vincent and Osborne*, 1993]. The direction of ripple migration has been related to the velocity skewness and, according to *Crawford and Hay* [2001], offshore (onshore) migrating ripples are related to negative (positive) short-wave skewness.

[6] Under conditions where sediment is not intermittently suspended or does not bypass ripples, the rates of bed form transport and bed load transport should be equal [*Huntley et al.*, 1991]. This assumption seems to hold for the lower shoreface [*Amos et al.*, 1999], but only a few studies have attempted to test it in shallower water. *Traykovski et al.* [1999] monitored ripple migration in 11 m water depth over a 6-week period and found that the *Meyer-Peter and Müller* [1948] equation underpredicted the observed bed load transport by at least 1 order of magnitude. It was suggested that the discrepancy between measured and predicted bed load transport arose because suspended transport also contributed to ripple migration. *Hay and Bowen* [1993] observed bed level changes over three successive storms in 2 m water depth and found that the bed load transport rates derived from migrating ripples were 2 orders of magnitude less than that predicted by the bed load equations of *Madsen and Grant* [1977] and *Watanabe* [1982]. Both studies also compared the ripple transport rate with observed suspended sediment fluxes. Suspended sediment transport during the study of *Traykovski et al.* [1999] was in the offshore direction (owing to vortex formation) and a factor 20 less than the bed load transport estimated from ripple migration. *Hay and Bowen* [1993] only measured the mean suspended flux (product of mean flow and mean sediment concentration) and found this to be 1 order of magnitude more than the ripple transport rate.

[7] All recent field studies have been conducted on either fine or medium sand substrates ($D_{50}$ = 0.125–0.5 mm), with ripple heights rarely exceeding 5 cm (the ripples monitored by *Crawford and Hay* [2001] were even less than 5 mm high). The characteristics of the bed material are, however, of fundamental importance in controlling ripple characteristics and behavior. The significance of the sediment size has been demonstrated by *Hay and Mudge* [2005], who, even after acoustically monitoring the sea bed for more than 70 days, not once captured long-crested vortex ripples in fine sediments (i.e., 0.2 mm median diameter). The only recent and in-depth study into ripple dynamics conducted in coarse sand is that of *Doucette* [2002a], who made visual observations of the sea bed evolution just seaward of the step on a coarse sandy beach ($D_{50}$ = 0.7 mm) over two sea-breeze cycles. The shore-parallel ripples, which were classified as orbital ripples, were characterized by a height and length of 0.05–0.15 m and 0.3–1.2 m, respectively, and migrated in the onshore as well as the offshore direction with rates of up to 0.2 cm min$^{-1}$.

[8] There thus exists a real grain size gap in the nearshore ripple literature and the purpose of this paper is to present and discuss observations of bed form dynamics obtained from the nearshore zone of a coarse sand beach. We will first describe the bed forms and evaluate the applicability of existing ripple classification schemes and predictive equations to explain their geometry and occurrence. Subsequently, we will present an extensive data set on ripple migration rates and relate these data to the hydrodynamic forcing. Finally, we will compare the sediment transport rate derived from migrating bed forms to bed load predictions and suspended sediment flux measurements.

## 2. Field Site and Instrumentation

[9] A 3-week field experiment was conducted on Sennen Beach, Cornwall, England. During the field campaign, morphological, sedimentological and hydrodynamic data were collected during 37 tidal cycles over a range of wave and tide conditions in May 2005. Sennen Beach is a 2-km-long embayed beach and the measurements reported here were conducted in the center of the embayment (Figure 1). The beach experiences a mean spring range of 5.3 m and has an average significant wave height of approximately 1.4 m [*Davidson et al.*, 1998]. The beach faces roughly west-northwest and is exposed to Atlantic swell, but also receives locally generated wind waves. The beach can be classified as a low-tide terrace beach [*Masselink and Short*, 1993], and is characterized by a steep upper part (tan $\beta$ = 0.08) and a gently sloping lower section (tan $\beta$ = 0.03). The transition between these two profile segments is located around the

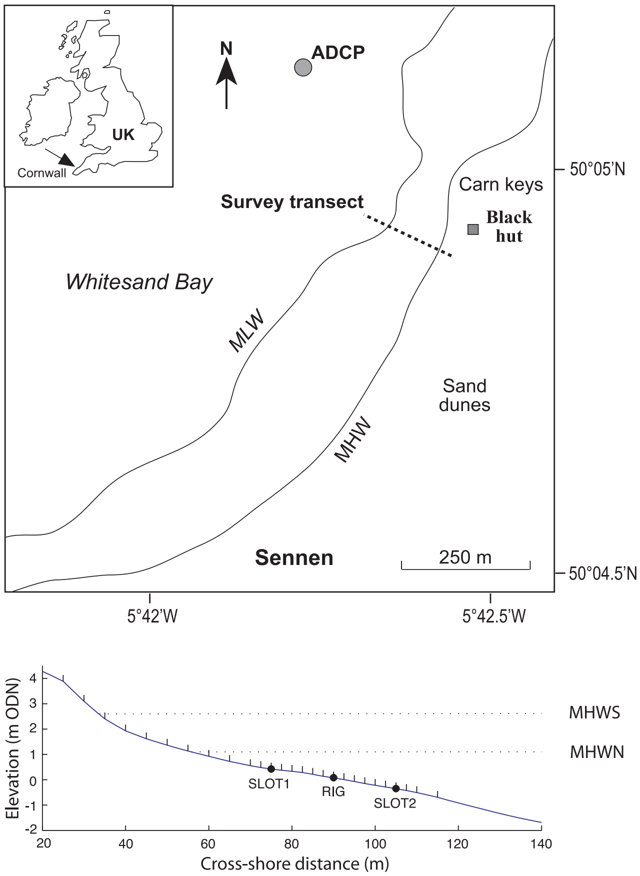


**Figure 1.** Location map and beach profile of Sennen Cove. (top) Map indicating the cross-shore instrument and survey transect and the offshore location of the ADCP; (bottom) beach profile with high tide levels, cross-shore position of the main (RIG) and auxiliary (SLOT) instruments, and the location of morphological and sedimentological sampling (vertical lines). ODN refers to Ordnance Datum Newlyn (approximate mean sea level datum for the UK), and MHWS and MHWN are the mean high water level during spring and neap tides, respectively.

mean high water neap (MHWN) level and the steep part of the beach profile is therefore mainly affected by high-tide swash processes. The size and settling velocity distribution of the bed material at the instrument location, determined for a single sample collected during low tide 19, using sieving and a settling tube, indicate a predominance of coarse sediments: the median sediment size and settling velocity were $D_{50}$ = 0.6 mm and $w_s$ = 8 cm s$^{-1}$, respectively (Figure 2). The mean sediment size over the entire beach and over the field period was 0.69 mm (s.d. 0.07 mm), computed from the analysis of over 700 sediment samples by *Masselink et al.* [2007], which suggests that the instrument location is reasonably representative of the beach as a whole.

[10] During the field survey, three instruments rigs were deployed in a cross-shore transect across the intertidal beachface. The middle (main) rig was located around midtide level, which approximately corresponds to mean sea level (MSL), such that over a tidal cycle it was exposed to periods of both breaking and shoaling waves. The auxiliary rigs (SLOTs) were located 15 m either side of the main rig. The bed form morphology was monitored across a 2-m-long cross-shore profile using two acoustic Sand Ripple Profilers (SRP) mounted 0.7 m above the bed (Figure 3). Frequent visual inspections of the bed using a mask and snorkel were made to confirm that ripples were predominantly two-dimensional. Each SRP collected one acoustic swath every minute with horizontal and vertical resolutions directly underneath the SRP of 0.012 m and 0.0083 m, respectively. A single-point altimeter was deployed 0.4 m above the bed to provide additional information on the bed level. Water velocity was measured using six miniature (0.032 m diameter discus head) Valeport electromagnetic current meters (ECM) deployed to record flow velocities at 0.03, 0.06, 0.09, 0.13, 0.19 and 0.29 m from the bed (Figure 3). The water depth was measured using a pressure transducer (PT) installed 0.02 m below the sand surface. Atmospheric pressure, recorded with an emerged PT, was subtracted from the calibrated data and the water depth was determined by assuming that a pressure of 0.01 Pa is equivalent to a 1 cm head of water. A vertical array of miniature optical backscatter sensors (OBS) were used to measure the suspended sediment concentration at

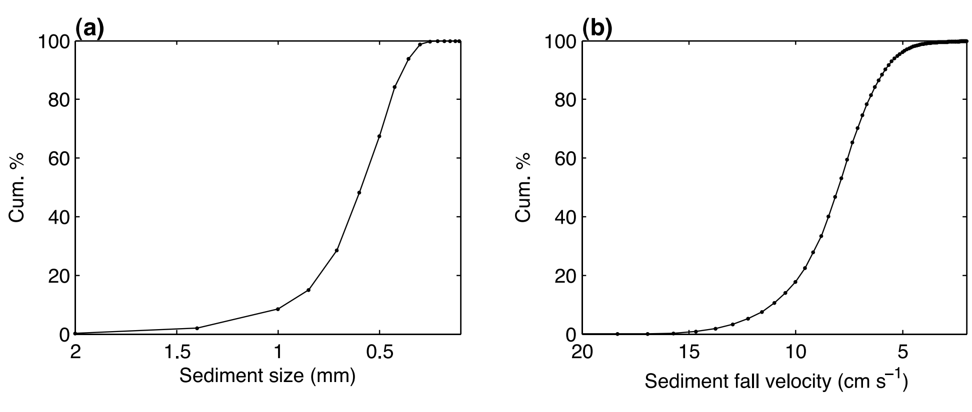


**Figure 2.** (a) Grain size and (b) sediment fall velocity distribution of sediment collected at the instrument location.

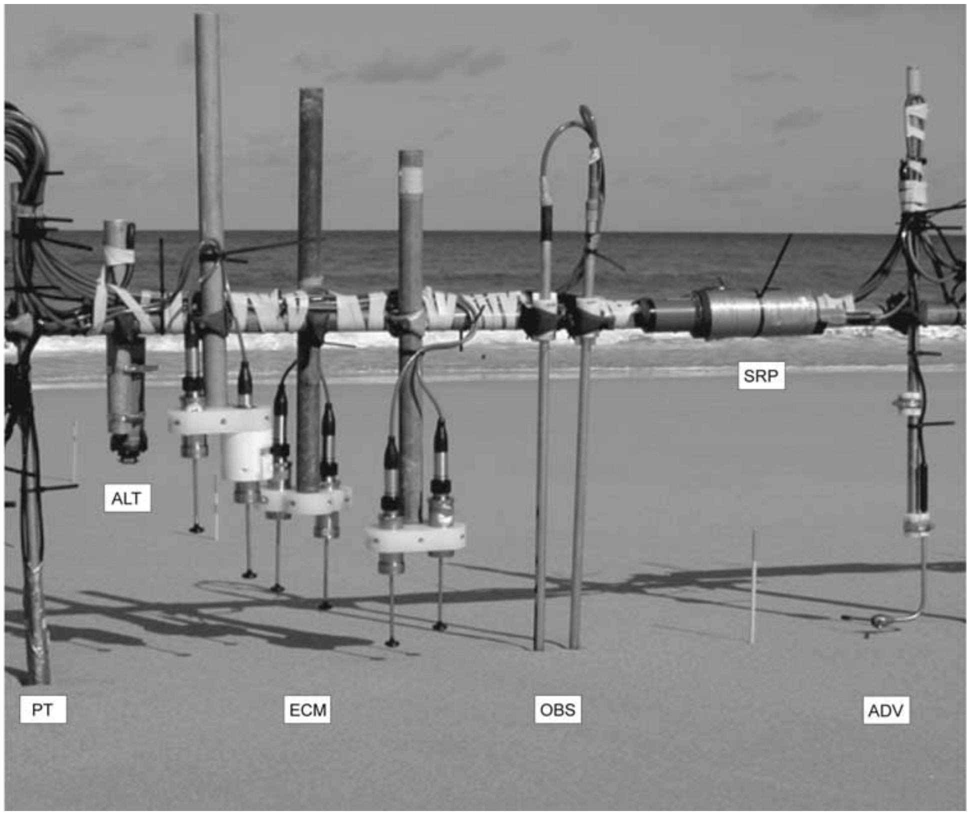


**Figure 3.** Photo showing the configuration of the sensors on the instrument rig (PT, pressure transducers; OBS, optical backscatter sensors; ECM, electromagnetic current meters; SRP, sand ripple profiler; ADV, acoustic Doppler Velocimeter; and ALT, altimeter). The ADV was not used in this study. The second SRP is mounted 1 m to the right and on the same rig as the SRP in the photograph. The horizontal separation between the OBS sensors and the most distant ECM was 70 cm.

−0.02, −0.01, 0, 0.01, 0.02, 0.03, 0.04, 0.05, 0.06, 0.09, 0.13 and 0.19 m from the bed. These were calibrated by suspending known quantities of local sediment in glycerol using the method developed by *Butt et al.* [2002]. The OBS data were adversely affected by sunlight and only data collected during night time could be used. The OBS sensors were also used to record bed level changes, because when individual sensors became buried by accretion, their output was maximum. All main rig instruments were cabled to shore-based computers where the hydrodynamic data were synchronously logged at 4 Hz. The SLOTs were self-logging and each incorporated an ECM, PT and OBS. Offshore wave conditions were measured throughout the field survey with an acoustic Doppler current profiler (ADCP) moored 1 km offshore in ~14 m water depth.

## 3. Data Processing, Analysis, and Description

### 3.1. SRP Data

[11] Within the nearshore region, a problem affecting acoustic instruments is the scattering and attenuation of the signal by bubbles and suspended sediment in the water column. Therefore a degree of initial processing was required in order to minimize noise from the signal prior to further analysis. An algorithm was developed on the basis of successively applying a temporal and spatial filter to the raw SRP data. First, the SRP swaths were visually checked; the swaths recorded at the start and end of a run were heavily contaminated by noise from the swash and inner surf zones and were discarded. The SRP stores data using an $x$-$z$ coordinate system ($x$ and $z$ are respectively the cross-shore distance and elevation below the SRP relative to its centreline) and this was converted to a range R and angle $\phi$ for processing. The next stage was to apply a temporal filter. A 5-min median filter was implemented whereby spurious bed-return pings were removed by setting the pings sampled at $t_n$ equal to the median of the pings sampled from swaths between $t_{n-2}$ and $t_{n+2}$. A spatial filter, implementing a three-point moving average, was then applied to smooth the swaths. The SRP swaths were corrected for any tilt in the sensor mounting and converted back to $x$-$z$ coordinates. The final stage of the preprocessing was to detrend the data and interpolate onto a cross-shore profile at 0.01 m intervals.

[12] There are two principal approaches to derive ripple geometry and dynamics: (1) identify individual ripples in the data and conduct ripple-by-ripple analysis and (2) apply standard time series analysis techniques to the spatial bed level data. The latter approach was favored here for reasons of expediency and objectivity, and is illustrated in Figure 4. Ripple length $\lambda$ was determined from the spatial lag corresponding to the strongest negative autocorrelation peak multiplied by two. This method works very well most of the time; however, occasionally, when ripples are irregular, the length is overpredicted by a factor of two. To overcome this

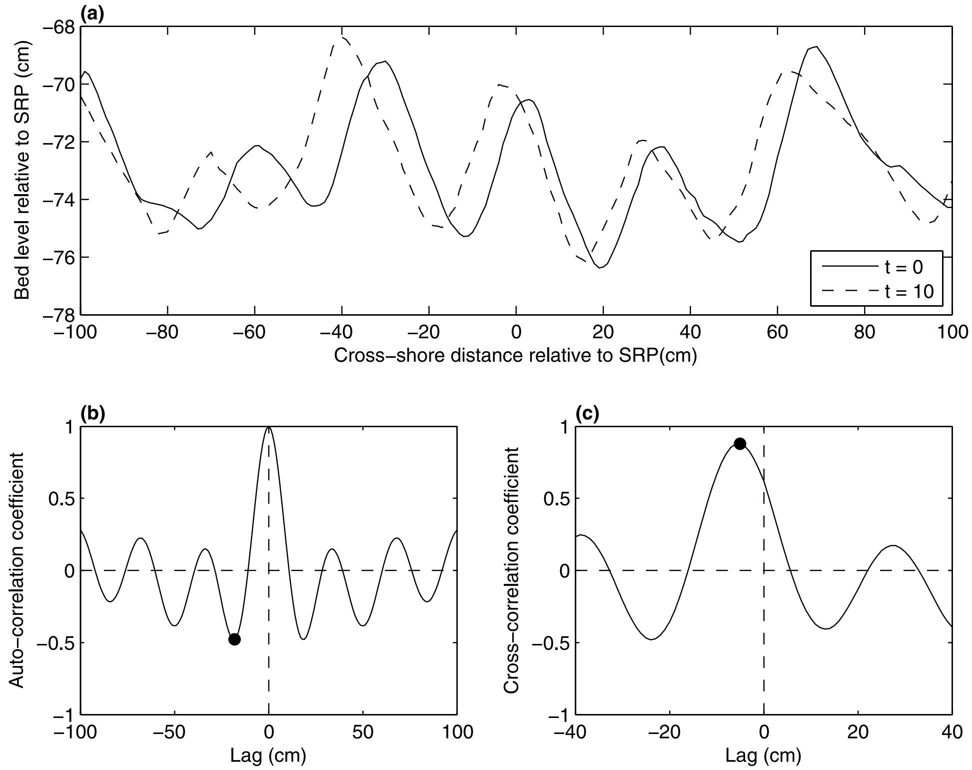


**Figure 4.** Derivation of ripple geometry and dynamics from SRP data. (a) Preprocessed SRP swaths recorded 10 min apart; (b) autocorrelation of the swath at $t$ = 0 indicating the strongest negative autocorrelation peak; and (c) cross correlation between the swaths with the strongest positive cross correlation, which represents the migration distance, marked.

problem the bed level profile was high-pass filtered using a cutoff twice the estimated ripple length. The ripple height $\eta$ was estimated as the root mean square wave height equivalent for ripples [e.g., *Crawford and Hay*, 2003] using $\sqrt{8}\sigma$, where $\sigma$ is the standard deviation of the bed level profile. Ripple steepness was given by the ratio of $\eta$ to $\lambda$. The crest asymmetry $\Gamma$ of the bed forms was defined as $\langle a_r^3\rangle/\langle a_r^2\rangle$, where $a_r$ is the derivative of the bed level profile and $\langle\rangle$ denotes time-averaging. This is analogous to the method used by *Hoefel and Elgar* [2003] to parameterize crest asymmetry in ocean waves. A positive (negative) value for $\Gamma$ indicates onshore (offshore) asymmetry. Ripple migration rate $M_r$ was determined using the cross-correlation function between two bed level time series recorded 10 min apart. The lag (in cm) associated with the strongest positive cross correlation was considered to represent the overall migration distance of the ripple field. This distance divided by 10 then provides the ripple migration rate in cm min$^{-1}$.

[13] During the 37 tidal cycles that data were collected, bed form observations were available from 18 tides spanning a large range of wave conditions (wave breaker height $H_b$ = 0.3–2 m) and nearshore locations (shoaling and surf). Two morphodynamic indices, the surf scaling parameter $\epsilon$ (=$2\pi^2 H_b/gT^2\tan^2\beta$) and dimensionless fall velocity $\Omega$ (=$H_b/w_sT$) were calculated and indicate that the beach state ranged from dissipative wave-dominated conditions conducive to the formation of nearshore bar morphology ($\Omega > 1$ and $\epsilon$ = 10–20) to intermediate/reflective conditions with plunging breakers and onshore sediment transport ($\Omega < 1$ and $\epsilon$ = 5–10) [*Masselink et al.*, 2007].

[14] The SRP recorded an acoustic swath every minute and ripple geometry and dynamics were calculated for each swath. The swaths were subsequently combined to produce 10-min block averages resulting in a total of 332 useable data segments. Of the remaining tides, the SRP was not active for the first eight, and during several periods of highly energetic waves, the SRP signal was irretrievably saturated with noise from waves plunging on the instrument rig.

[15] The temporal evolution of the ripples during a ~3-hour period over the high tide of Tide 19 is illustrated by Figure 5, which shows the postprocessed SRP swaths, ripple height, length, steepness, asymmetry and migration rate (the coincident hydrodynamic data are shown in Figure 6). Tide 19 was chosen since it was one of the few with coincident hydrodynamic, suspended sediment and ripple data for the entire tide. The ripples undergo a brief phase of growth during the first 30 min of the 3-hour period when $\eta$ and $\lambda$ gradually increase; subsequently, ripple geometry stabilizes. The mean ripple height and length were 5.5 cm and 35 cm, respectively, giving a steepness of ~0.16 and the ripples were onshore asymmetric. The ripple migration rate $M_r$ indicates three distinct dynamic phases: (1) during the initial 30 min growth phase, the ripples migrate rapidly onshore at $M_r$ = 0.5–1.5 cm min$^{-1}$; (2) over the subsequent 2 hours, migration remains constantly onshore with $M_r$ = 0.25 cm min$^{-1}$; and (3) during the final 30-min migration increases to $M_r$ = 0.5–1 cm min$^{-1}$.

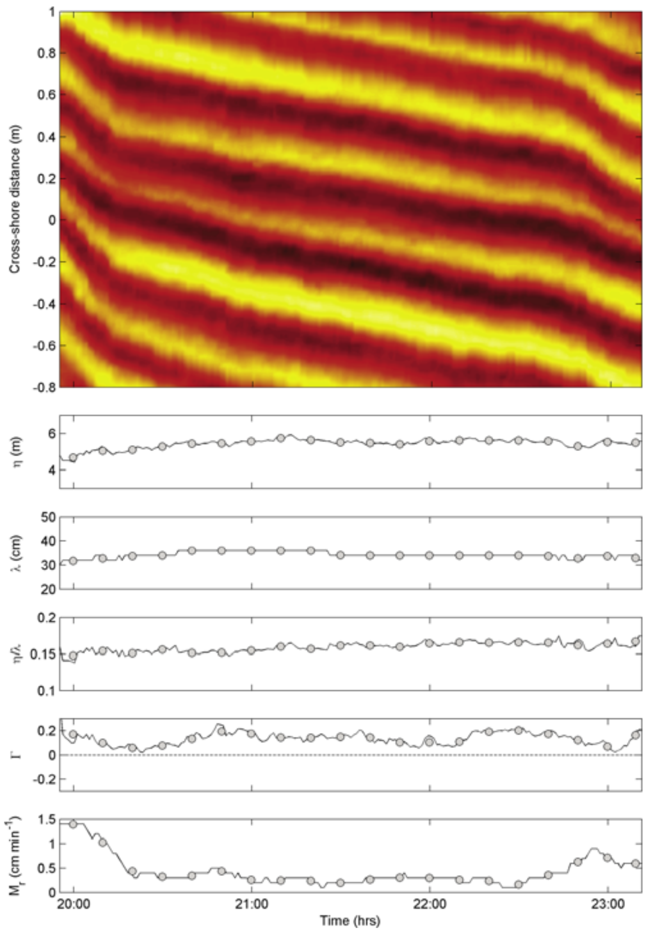


**Figure 5.** Bed form evolution during a ~3-hour period over the high tide of Tide 19. (top) Surface diagram of bed forms obtained from the SRP swaths. The color scale indicates ripple elevation, with light and dark shading denoting ripple crests and troughs, respectively, and offshore is toward the top. The line graphs show the corresponding evolution of: ripple height $\eta$, wavelength $\lambda$, steepness $\eta/\lambda$, asymmetry $\Gamma$, and migration rate $M_r$. Solid lines indicate the ripple geometry calculated for each SRP swath, and the solid circles are the 10-min block averages.

These migration rates consistently exceed those reported by *Crawford and Hay* [2001, Figure 12] and *Traykovski et al.* [1999, Figure 14] and are probably due to the shallower water depths experienced during this study and the consequently stronger wave-driven oscillatory flows.

### 3.2. Hydrodynamic Data

[16] The continuous data collected by the hydrodynamic instruments (time series of water depth $h$ and cross-shore flow velocity $u$) were calibrated, despiked and organized into 10-min segments corresponding to the ripple parameters. The time series of $u$, measured 6 cm above the bed, was used to calculate the maximum orbital velocity $U_m$ (=$2\sigma_u$, where $\sigma$ represents the standard deviation of $u$), the mean flow velocity $\langle u\rangle$ (where the brackets denote time-averaging), velocity skewness $\langle u^3\rangle$ and the acceleration skewness $a_{spike}$(=$\langle a^3\rangle/\langle a^2\rangle$, where $a$ is the time series of acceleration). Using the hydrodynamic indicators above, the Mobility number $\psi$ and Shields parameter $\theta$ were computed

$$\psi = \frac{U_m^2}{(s-1)gD} \tag{1}$$

$$\theta = \frac{0.5 f_w U_m^2}{(s-1)gD}, \tag{2}$$

where $s$ the specific gravity of sand and $g$ is the gravitational acceleration. The wave friction factor $f_w$ is defined as [*Swart*, 1974]

$$f_w = \exp\left[5.213(k_s/A)^{0.194} - 5.977\right], \tag{3}$$

where $k_s$ is the Nikuradse roughness length defined as $k_s$ = 2.5 $D$, and $A$ the wave orbital amplitude. The presence of a rippled bed causes a velocity enhancement as flows pass over ripple crests. The boundary layer is compressed at the crests with the result that there is an increase in the bed stress and therefore sediment transport. *Nielsen* [1992] proposed a velocity enhancement factor of $1/(1-\pi\eta/\lambda)$ and the enhanced Shields parameter $\theta_*$ is given by

$$\theta_* = \frac{\theta}{(1-\pi\eta/\lambda)^2}. \tag{4}$$

[17] An example of the cross-shore hydrodynamics for Tide 19 (note that this is the same tide for which the ripple dynamics were discussed and presented in Figure 5) is provided in Figure 6. While the significant wave height $H_s$ (=$4\sigma_h$, where $\sigma_h$ is the standard deviation of the hydrostatic pressure record) remained constant at 0.35 m during the period, the tidal modulation of $h$ caused the relative position of the instrument rig to vary over the tide. The relative cross-shore position of the instrument rig can be quantified in terms of the relative wave height $H/h$ [*Ruessink et al.*, 1998]. This parameter varies from $H/h$ = 0.6–0.8 at the start and end of the run when the rig was located in the surf zone, to $H/h \approx 0.2$ over the high tide when the rig is seaward of the surf zone and subjected to shoaling waves. The change in the location of the rig relative to the different hydrodynamic zones is manifest in the flow velocity parameters: $U_m$ and $\theta$ peak around 2000 hours and 2300 hours, and $\langle u^3\rangle$ and $a_{spike}$, which parameterize vertical and horizontal wave deformation, respectively, are also maximum in the surf zone. The presence of ripples with a steepness $\eta/\lambda \simeq 0.16$ during Tide 19 results in a bed stress enhancement of a factor 4 when $\theta_*$ and $\theta$ are compared. This implies that the presence of a rippled bed will result in greater transport, and particularly suspension, of sediments compared to the plane bed situation.

[18] The relative wave height will play an important role in the subsequent cross-shore parameterization of bed form migration. It conceptually indicates the relative importance of a number of cross-shore processes, including mean cross-shore flows, wave orbital velocity, flow-sediment correlation and wave deformation [*Plant et al.*, 2001]. Here, on the relatively steep beach at Sennen, we define the transition

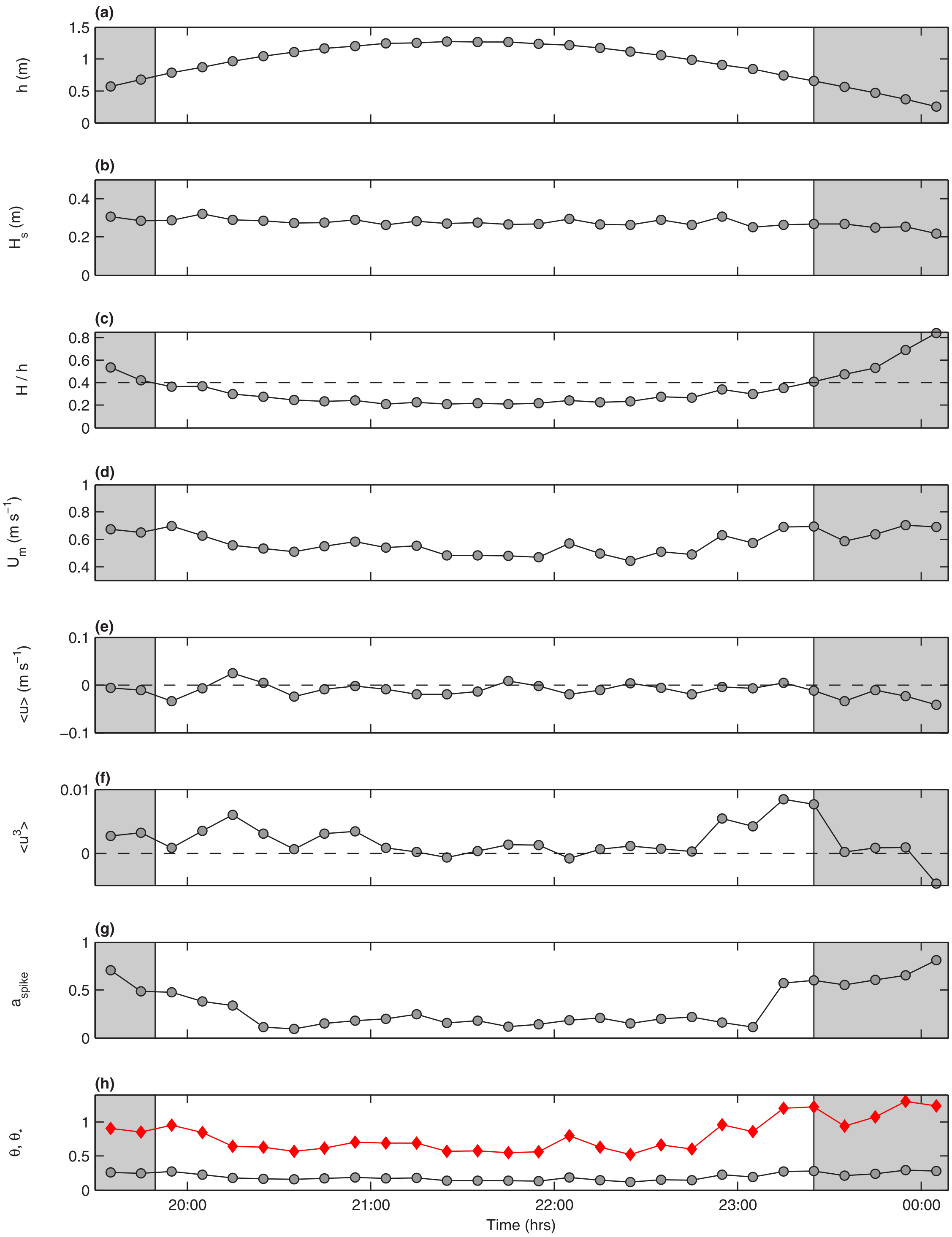


**Figure 6.** Example hydrodynamic time series recorded during Tide 19: (a) water depth $h$; (b) significant wave height $H_s$; (c) relative wave height $H/h$; (d) maximum cross-shore orbital velocity $U_m$; (e) mean cross-shore velocity $\langle u \rangle$; (f) velocity skewness $\langle u^3 \rangle$; (g) acceleration skewness $a_{spike}$; and (h) the Shields parameter $\theta$ (circles) and enhanced Shields parameter $\theta_*$ (triangles) suggested by *Nielsen* [1992]. The shaded regions represent surf zone data indicated by the horizontal dashed line in Figure 6c which marks the start of the surf zone at $H/h$ = 0.4.

from shoaling to surf zone, the 'breaker zone', to occur at $H/h$ = 0.4–0.5, encompassing the range of values reported by *Thornton and Guza* [1982], *Smith and Kraus* [1991] and *Plant et al.* [1999].

[19] Comparing Figures 5 and 6 reveals a strong link between $M_r$ and the hydrodynamic forcing: when the forcing is greatest at the beginning and end of the run, the ripples migrate rapidly compared to the more quiescent

period over the middle of the run. This observation is similar to findings of *Traykovski et al.* [1999] and *Crawford and Hay* [2003], who both found a positive correlation between $M_r$ and $\langle u^3 \rangle$; however, the importance of the position of the ripples relative to the breakpoint requires further investigation and will be examined in section 5.

### 3.3. Suspended Sediment Data

[20] Data obtained by the OBS sensors required a significant amount of preprocessing prior to computing the suspended sediment concentrations and fluxes. The two main issues are contamination by daylight and changing bed levels. Data runs severely affected by daylight are easily spotted by their large offset values and saturated sensor outputs, and were discarded from the analysis. Data collected around dawn and dusk are only moderately affected by daylight and are characterized by a small nonzero offset that progressively increases (sunrise) or decreases (sunset) with time. These data were corrected by deriving a time series of the offset based on 1-min data segments based on the 10% exceedence of the suspended sediment concentrations, and subtracting the offset time series from the suspended sediment data. Changes in the bed level were determined through careful inspection of the OBS data, in conjunction with the data collected by the stack of current meters, the single-point altimeter and the SRP. Using the combined data set, a time series of the bed level at the location of the OBS sensors and current meters was derived, and this time series was subsequently used to correct the bed elevations of these sensors following *Austin and Masselink* [2007]. Linear interpolation was then used to obtain time series of $u$ and $c$ at 1-cm intervals above the local (i.e., intraripple) bed over the lower 15 cm of the water column; therefore, while the absolute elevation of the sensors changes over time, they remain at a constant elevation above the local bed. The adjusted time series were used for all subsequent analysis.

[21] The data were organized into 10-min segments and time series of $u$ and $c$ were used to compute the net suspended flux $q_{net} = \langle uc \rangle$, the mean (current-related) suspended flux $q_{mean} = \langle u \rangle \langle c \rangle$ and the oscillatory (wave-related) suspended flux $q_{osc} = \langle u'c' \rangle$, where the brackets denote averaging and $u'$ and $c'$ represent the fluctuating (demeaned) components of $u$ and $c$ [cf. *Jaffe et al.*, 1984]. The total suspended fluxes (net, mean and oscillatory) were obtained by summing over the lower 15 cm of the water column. Further investigation of the oscillatory flux component was conducted by computing the cospectrum between current velocity and sediment concentration [*Huntley and Hanes*, 1987].

[22] An example of the suspended sediment data analysis using data from Tide 19 is provided in Figure 7. The corresponding bed form and hydrodynamic data were discussed previously (refer to sections 3.1 and 3.2). Very modest wave conditions prevailed during Tide 19, with $H_s$ = 0.25–0.3 m. For most of the time, the main instrument rig was under the influence of shoaling waves and at high tide $h$ = 1.2 m. SRP data are available for most of the run and indicate onshore migration of ripples with a height of 4–6 cm and a wave length of 30–35 cm at rates of *c*. 1 cm and *c*. 0.3 cm min$^{-1}$ in the surf zone and under shoaling waves, respectively (refer to Figure 5). Over practically the entire data run, the net suspended sediment flux was $O$ (0.01 kg m$^{-1}$ s$^{-1}$) and in the onshore direction. The mean suspended flux, attributed to the weak offshore-directed mean flows, was in the offshore direction, but was secondary to the onshore-directed oscillatory suspended flux. The raw time series of $u$ and $c$, both measured at 0.03 m from the bed, and the cospectrum between these two signals clearly indicate that maximum suspended sediment concentrations coincide with the onshore phase of the wave-oscillatory currents and show offshore transport at infragravity frequencies. The enhanced suspension during the onshore stroke of the wave appears unrelated to the larger onshore than offshore flow velocities (i.e., skewness), but may be associated with the large positive flow accelerations at the front of the wave (i.e., wave asymmetry). Two additional factors are worth noting: (1) the sediment in suspension cannot be significantly finer than the median bed sediment, since there is very little fine material available (greater than 95% of the bed sediment has a fall velocity in excess of 5 cm s$^{-1}$) and; (2) sediment suspension is intermittent; therefore a time-averaged shear stress, based on $U_m$, will not be a good indicator of whether sediment suspension occurs. Sediment is generally entrained during the peak onshore phase of the flow and these peak velocities (bed shear stresses) are greater than the time-averaged velocities.

[23] Another interesting feature in the data is the tidal asymmetry in the suspended sediment concentration. During the ebb tide, the concentration of suspended sediments is greater than during the flood and is probably related to the time history of the bed morphology [*Davidson et al.*, 1993; *Masselink and Pattiaratchi*, 2000]. Comparison with the time series of ripple geometry (Figure 5) indicates that ripple height increases from 4.5 cm to 6 cm during the tide, thereby suggesting that the elevated ebb tide suspended sediment concentrations are a legacy of an increase in bed roughness.

[24] Interpolated vertical suspended sediment profiles were computed over the lower 15 cm of the water column for the four intervals indicated in Figure 7, and the mean, oscillatory and net suspended sediment flux profiles $q$ were calculated as the product of $u$ and $c$ (Figure 8). Hydrodynamic conditions were energetic at the beginning of the tide ($\theta$ = 0.3) and the ripples least developed ($\eta/\lambda$ = 0.15). Mixing length scales computed for each interval were $O$ (5 cm) and, as expected, similar to the ripple height. Throughout the tide there was an increase in near-bed sediment concentration from 1.5 to 4.4 kg m$^{-3}$, with a coincident increase in ripple steepness ($\eta/\lambda$ = 0.17). Net and oscillatory sediment fluxes were onshore-directed over the lower 15 cm over the water column and display a similar vertical and temporal distribution to $c$. Mean suspended fluxes were secondary to the oscillatory fluxes and were directed offshore. The vertical profiles of $c$ and $q$ support the suggestion that increased ripple development and hence bed roughness during the ebb tide results in elevated sediment concentrations and fluxes.

## 4. Ripple Occurrence and Geometry

[25] Similar to previous field investigations in sandy nearshores [*Vincent and Osborne*, 1993; *Thornton et al.*, 1998; *Hanes et al.*, 2001], our observations of the bed

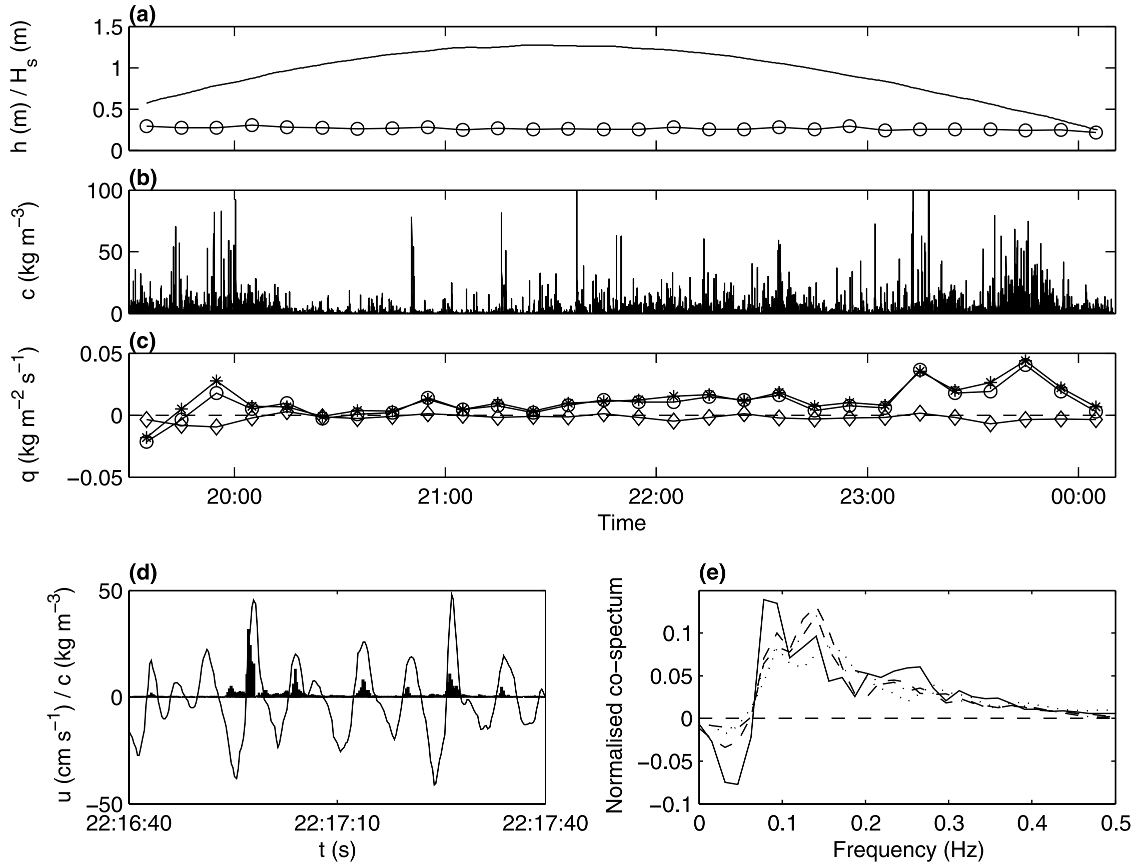


**Figure 7.** Example of suspended sediment data analysis during Tide 19. Time series of: (a) wave height $H_s$ (circles) and water depth $h$ (line); (b) suspended sediment concentration 3 cm above the bed; (c) net (circles), mean (diamond) and oscillatory (star) suspended flux over the lower 15 cm of the water column; (d) 1-min raw time series of cross-shore current velocity $u$ and $c$ at 3 cm above the bed; and (e) cospectra between $u$ and $c$ recorded at four time intervals: 2000–2100 (solid line), 2100–2200 (dashed line), 2200–2300 (dash-dotted line) and 2300–0000 (dotted line).

morphology fall into two main classes: "small" wave ripple forms (SWR) with wave lengths less than 0.5 m and "large" wave ripple forms (LWR) with wave lengths larger than 0.5 m (including plane bed). The overwhelming majority of the ripples observed were SWR; LWR and plane bed conditions were only observed on a few occasions, under quite energetic surf zone conditions during which the SRP struggled to return a reliable image of the sea bed. The present analysis will therefore focus on the small ripple type, although occasional reference will be made to the large ripple and plane bed data.

[26] All 10-min observations of the bed morphology collected throughout the field survey have been summarized by histograms of the different geometric ripple parameters in Figure 9. The histograms have been normalized by dividing the number of counts in each class by the total number of bed form observations multiplied by the class width, such that the integrated area under the histogram equals unity. Ripple heights range from 3 to $\sim$10 cm, and the lengths from 23 to 70 cm. The steepness, which is approximately Normally distributed around 0.16, indicates that the observed bed forms are classical vortex ripples. Ripple crest asymmetry indicates mildly onshore-asymmetric bed forms where the landward (seaward) slope is of steeper (shallower) gradient.

[27] Ripple classification schemes have focused on the factors that determine the length and height scales of wave-formed ripples using similar scaling factors across a range of conditions. For example, *Clifton and Dingler* [1984], found ripple length scaled linearly with orbital diameter until orbital diameter/grain size ($d_o/D$) reached 2000; these were termed orbital ripples. Between $2000 < d_o/D < 5000$, the ripples are in a transitional state, during which they are termed suborbital. At values of $d_o/D > 5000$, the bed forms are anorbital and scale directly with grain size. *Wiberg and Harris* [1994] classify ripple type on the basis of the ratio of near-bed orbital diameter to ripple height. Following this classification, the transition from orbital to anorbital ripples occurs when the boundary layer thickness increases above the ripple height.

[28] Figure 10a plots $\lambda$ against $d_o$, nondimensionalized by the grain diameter, and indicates *Clifton*'s [1976] subdivision of ripples into three types based on the relationship between ripple spacing and orbital diameter.The ripples recorded at Sennen are predominantly suborbital, for which the ripple spacing depends on both $d_o$ and $D$; however, above $d_o/D$ values of $\sim$5000, where ripple spacing becomes independent of the orbital excursion, some anorbital ripples exist. The plot of ripple steepness $\lambda/\eta$ against $d_o/D$ confirms the earlier suggestion of vortex ripples (Figure 10b). As

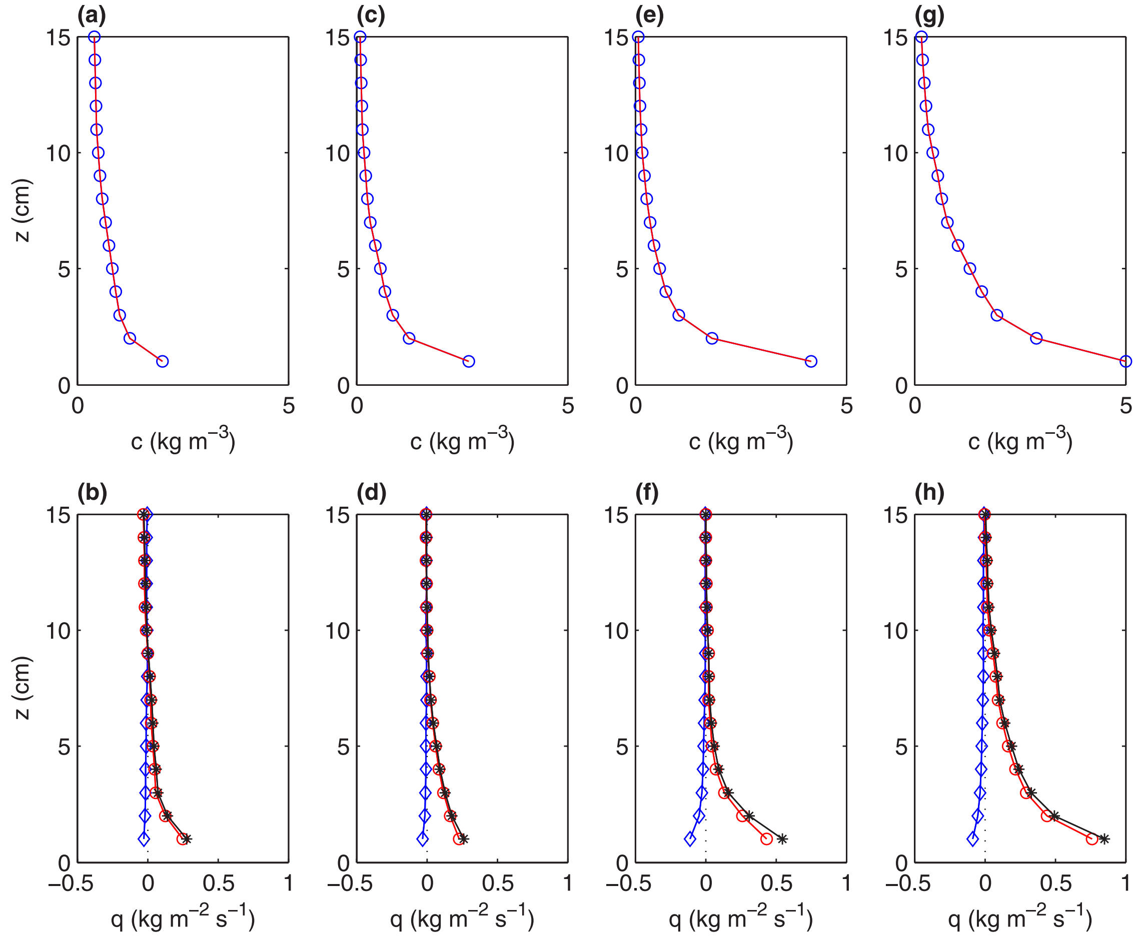


**Figure 8.** Example vertical profiles of suspended sediment concentration $c$ and flux $q$ over the lower 15 cm of the water column recorded at four time intervals during Tide 19: (a, b) 2000–2100, (c, d) 2100–2200, (e, f) 2200–2300 and (g, h) 2300–0000. The flux is separated into net (circles), mean (diamond), and oscillatory (star) components.

orbital diameters increase, there is a tendency for the ripples to progress toward being anorbital, but in contrast to *Clifton and Dingler* [1984], who find the transition to anorbital ripples is accompanied by the change to postvortex ripples, the ripples at Sennen remain almost exclusively vortex ripples.

[29] As an alternative scaling, including the effects of the sediment characteristics, the ripple geometry is plotted as a function of the near-bed Mobility number $\psi$ (Figure 11). Overall, there is a large degree of scatter using this scaling, hence the log scales, but relationships exist between $\psi$ and ripple length ($r^2 = 0.35$) and height ($r^2 = 0.21$); however, the ripples separate into two fairly distinct groups. At low to moderate values of $\psi$, ripple dimensions gradually increase, but as $\psi$ rises above $\psi = 45$ there is a notable increase in $\eta$, $\lambda$ and overall scatter. This may be a reflection of the early development of plane bed or LWR conditions in the surf zone, similar to the findings of *Saulter et al.* [2003] who find the transition from SWR to LWR occurs at $\psi = 80$ and the onset of plane bed conditions at $\psi = 100$.

[30] Various studies have attempted to predict ripple geometry using a range of independent variables. Here we compare our field measurements of ripple geometry with the empirical models of *Nielsen* [1981] and *Wiberg and Harris* [1994]. The *Nielsen* [1981] model uses the near-bed orbital semiexcursion $A$ and the Mobility number $\psi$ to predict ripple height and length under irregular waves [cf. *Osborne and Vincent*, 1993; *Hanes et al.*, 2001]. In addition, *Nielsen* [1981] uses the Shields parameter $\theta$, to independently fit curves for ripple steepness. The formulation of *Malarkey and Davies* [2003], which redefines the *Wiberg and Harris* [1994] model in a noniterative form, is used here.

[31] Following the method of *Hanes et al.* [2001], the relative error $\Delta$ between the measured ripple geometry and the values predicted using the *Wiberg and Harris* [1994] and *Nielsen* [1981] models can be defined as

$$\Delta = \exp\left\{\left[(1/n)\sum_{1}^{n}(\ln(y) - \ln(\hat{y}))^2\right]^{0.5}\right\}, \qquad (5)$$

where $\hat{y}$ is the measured value and $y$ the predicted value. The error is a multiplicative factor that indicates the variation about the predicted value. For example, if $\Delta$ equals 1.56, the average error is 56%. Table 1 shows the relative error between the measured and predicted ripple dimensions. The *Nielsen* [1981] model provides a very poor prediction for $\eta$ and $\lambda$ with relative errors of 3.26 and 3.3 respectively, but provides a reasonable estimate of $\eta/\lambda$ with

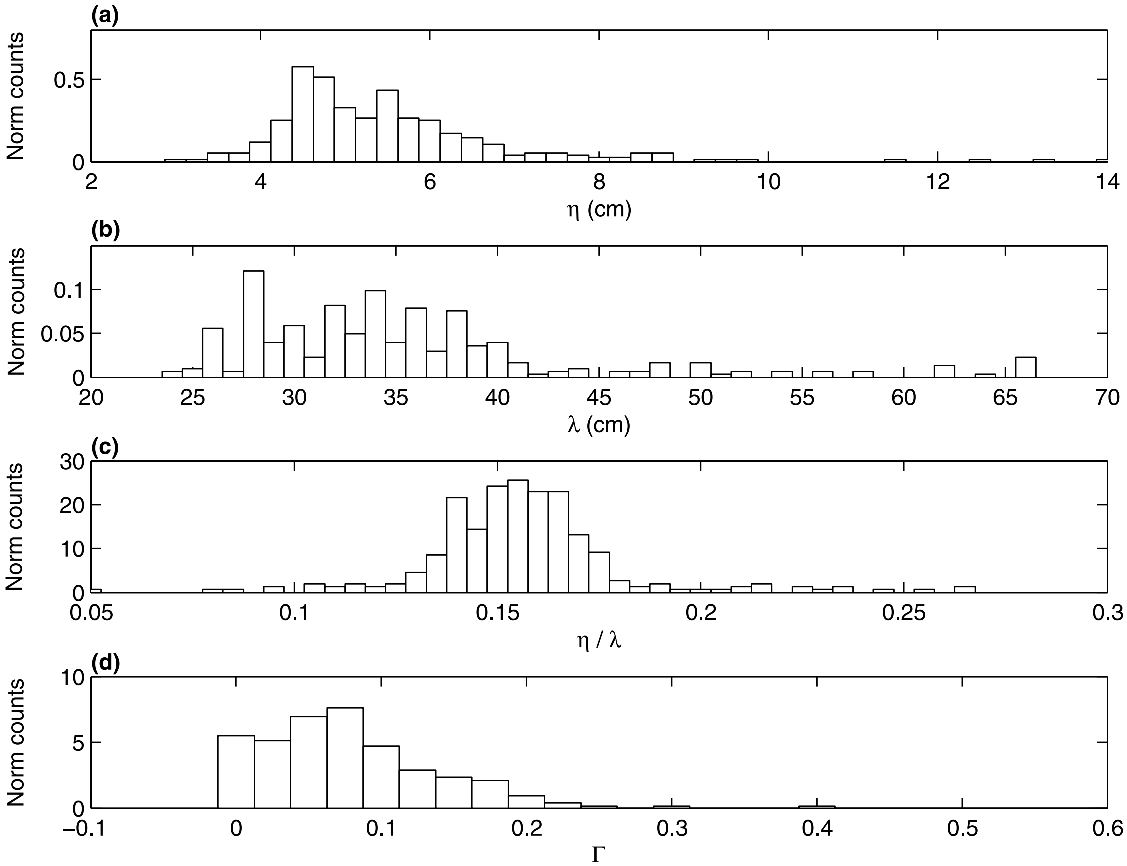


**Figure 9.** Normalized histograms for ripple: (a) height $\eta$; (b) length $\lambda$; (c) steepness $\eta/\lambda$; and (d) asymmetry $\Gamma$.

$\Delta$ = 1.29. The *Wiberg and Harris* [1994] model performs better with relative errors of 2.59 and 2.37 for height and length, respectively, and the estimate of ripple steepness is good with a relative error of 1.20. The poor performance of both models at predicting ripple height and length is attributed to the coarseness of the sediment and the conditions under which the models were formulated. Both models were formulated for medium sand beaches and are heavily based on the results of small-scale laboratory experiments. However, previous observations with field-scale orbital amplitudes, have demonstrated poor correlation between measured and predicted data [e.g., *Osborne and Vincent*, 1993; *Doucette*, 2002a], which can only be exacerbated by the coarse grain size at Sennen.

## 5. Ripple Migration

[32] The migration rate $M_r$ was determined from the cross correlation of bed-level time series recorded at 10-min intervals (section 3.1) and is measured normal to the ripple crests. The direction of migration is either onshore or offshore since the ripple crests are assumed to be aligned shore parallel (visual observations indicated that the angle between wave ripples and the shoreline was always less than 30°). Time series of $M_r$, (refer to Figure 5), indicate that ripple migration may be correlated with various hydrodynamic parameters such as $\psi$ and $\langle u^3 \rangle$, in agreement with the findings of *Vincent and Osborne* [1993] and [*Crawford and Hay*, 2003]. A least squares analysis was performed between $M_r$ and the hydrodynamic parameters defined in section 3.2. Owing to the differing behavior of ripples close to the breakpoint observed in Figures 5 and 6, the measured ripple population was separated into shoaling and surf zone subsamples using $H/h$, and regression analysis was conducted on each group individually; the results, together with those for just Tide 19, are shown in Table 2. It is clear that none of the parameters are able to satisfactorily predict $M_r$ for either the entire population of ripples or those observed in the surf zone; however, their skill increases when considering just those ripples observed during shoaling. $U_m$ and $\langle u^3_{shortwave} \rangle$ explain 34% and 42% of the migration rate variance, respectively, while the dimensionless parameters $\psi$ and $\theta$, which are largely based on $U_m$, explain 20–32%. Of particular note is the poor performance of $\langle u^3 \rangle$, in direct contrast to the findings of *Crawford and Hay* [2003] who reported a correlation between $M_r$ and $\langle u^3 \rangle$ of better than 0.7. Note, however, that the data described by *Crawford and Hay* [2003] represent a single storm event, whereas the present data set includes a large number of tidal cycles. Selection of a single tidal cycle from our data set, T19, produces higher correlations between $M_r$ and the hydrodynamic parameters than for all the data combined. The two parameters able to explain the most variance for the whole data set and, indeed, for the T19 data set, are the relative wave height $H/h$ ($r^2$ = 0.66) and acceleration skewness $a_{spike}$ ($r^2$ = 0.58).

[33] The relationship between the nearshore location, parameterized by the relative wave height $H/h$, and $M_r$

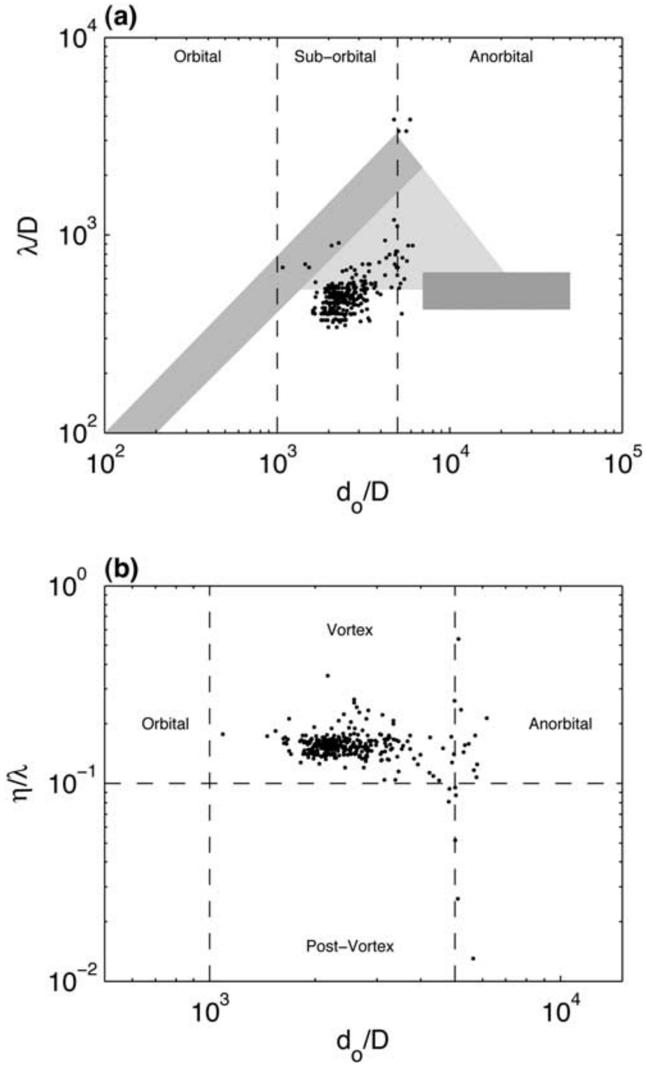


**Figure 10.** Ripple observations placed within the ripple classification scheme of *Clifton and Dingler* [1984].

and several wave-current parameters is further explored in Figure 12. In the shoaling wave region ($H/h$ < 0.4), all parameters fall within a relatively narrow band with $\theta$, $a_{spike}$ and $M_r$ increasing landward and $\langle u \rangle$ remaining consistently low. At the breakpoint ($H/h$ = 0.4–0.5) their behavior changes and $\theta$, in particular, rapidly increases in the onshore direction, and $\langle u \rangle$ becomes negative. At the same time, the scatter in $M_r$ increases dramatically and even includes offshore migration rates.

[34] The results illustrated in Figure 12 and Table 2 suggest that the migration rate of suborbital vortex ripples across the nearshore cannot simply be related to the energy level of the hydrodynamic forcing, but is strongly dependant on their location relative to the breakpoint. Seaward of the surf zone, ripples migrate onshore forced by a combination of orbital velocity ($U_m$, and the related $\theta$, etc.) and wave asymmetry effects ($a_{spike}$). However, for the entire data set, these parameterizations perform poorly owing to the variation in energy levels over the fieldwork period. For example, $U_m$ recorded close to the breakpoint under calm conditions may be the same as that recorded in the outer shoaling zone during a storm, but the ripple migration rates in the former case are expected to be less than in the latter case. The relatively low migration rates in the surf zone are attributed to the offshore-directed mean flows [*Doucette*, 2002b], the velocity of which are generally an order of magnitude greater than $M_r$.

## 6. Bed Load Transport

[35] The ripple migration rate can provide an estimate of the sediment transport rate and direction under waves in the nearshore. The mean transport associated with the migrating ripples $Q_b$ can be estimated as

$$Q_b = 0.5(1-p)\rho_s \eta M_r, \qquad (6)$$

where $p$ is the sediment porosity, $\rho_s$ the sediment density (2650 kg m$^{-3}$ for quartz sand) and $\eta$ the ripple height. The transport due to ripple migration was calculated for every 10-min section of data and implicit in this method is the assumption that ripple geometry remained constant during each section. Figure 13 compares the estimated transport rate due to ripple migration with that calculated using the formulation for bed load transport under waves of [*Ribberlink*, 1998]

$$Q_{RIB}(t) = m(|\theta'(t)| - \theta_c)^n \frac{\theta'(t)}{|\theta'(t)|} \rho_s \sqrt{(s-1)gD^3}, \qquad (7)$$

where $\theta'(t)$ is an instantaneous Shields parameter suitable for spectral waves with nonzero skewness computed following *Nielsen* [1992]

$$\theta'(t) = \frac{1}{2} \frac{f_{2.5} u(t) \sqrt{|u(t)|^2 + |v(t)|^2}}{gD(s-1)}, \qquad (8)$$

where $\theta_c$ is the critical Shields value ($\theta_c$ = 0.05), $u$ and $v$ are the cross-shore and longshore flow velocity, respectively, $m$ and $n$ are coefficients, where $m$ = 11 and $n$ = 1.65 according to *Ribberlink* [1998] and $D$ is the median grain size. The bed load transport $Q_{RIB}$ was then averaged over each 10-min burst. The values of $Q_b$ recorded at Sennen (0.0007–0.08 kg m$^{-1}$ s$^{-1}$) are, as expected, significantly greater than those reported from the inner continental shelf by *Amos et al.* [1999] [0.00007 kg m$^{-1}$ s$^{-1}$] and around an order of magnitude greater than the mean value measured in the nearshore by *Hay and Bowen* [1993] (0.0002 kg m$^{-1}$ s$^{-1}$); however, they compare well to the reported rate of *Osborne and Vincent* [1993] (0.0035–0.013 kg m$^{-1}$ s$^{-1}$). According to this study, the Ribberink bed load transport model underpredicts ripple transport in the nearshore zone by about one order of magnitude ($r^2$ = 0.09). This is probably due to the significant contribution of suspended fluxes to the ripple transport, combined with the relatively large bed shear stresses.

## 7. Suspended Sediment Fluxes

[36] During all runs with reliable SRP data, wave ripples migrated onshore when under the influence of shoaling waves. The ripple migration rate was found to increase up

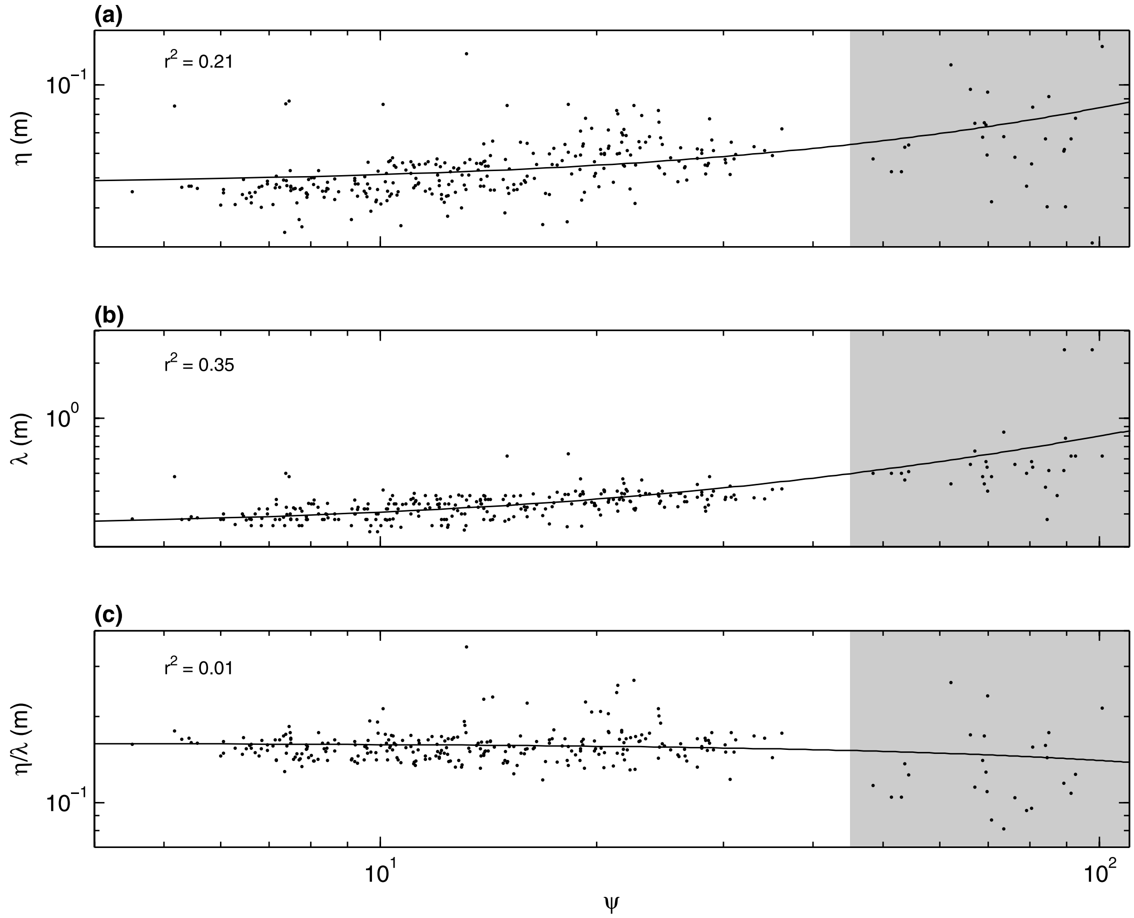


**Figure 11.** Ripple geometry as a function of the near-bed mobility number $\psi$ with solid lines indicating linear regression between the data. The shaded region indicates the higher energy population of ripples at $\psi > 45$.

to the wave breakpoint and the sediment transport rates associated with ripple migration were an order of magnitude greater than those predicted by the *Ribberlink* [1998] bed load transport model. It is of interest and significance to compare these ripple transport rates to the suspended fluxes, and to determine whether the migrating ripples contribute significantly to the total sediment transport. In the case of the data collected during Tide 19, discussed previously, the ripple transport rates were 0.01 kg m$^{-1}$ s$^{-1}$ near the wave breakpoint and 0.001 kg m$^{-1}$ s$^{-1}$ under shoaling waves. The corresponding total suspended fluxes were 0.03 and 0.01 kg m$^{-1}$ s$^{-1}$, respectively. This indicates that, at least for this particular data run, the ripple transport rates are clearly secondary to the suspended fluxes; however, they remain significant.

**Table 1.** Relative Error Between Measured and Predicted Ripple Dimensions

| Geometry | *Nielsen* [1981] | *Wiberg and Harris* [1994] |
|---|---|---|
| $\eta$ | 3.26 | 2.59 |
| $\lambda$ | 3.3 | 2.37 |
| $\eta/\lambda$ | 1.29 | 1.20 |

[37] All ripple and suspended flux data collected during the field campaign were used to investigate the contributions of ripple transport and suspension transport to the total sediment flux. The data were considered in 10-min segments and 591 suspended flux data segments and 144 ripple data segments were included (Figure 14). It is noted that the ripple and suspended flux data segments are not concurrent (no daylight suspended flux data and very limited surf zone ripple data).

**Table 2.** Results of Least Squares Analysis Between Ripple Migration Rate and Hydrodynamic Parameters for Tide 19, for All Data, and Split Into Shoaling and Surf Zone Regions

| | $r^2$ | | | |
|---|---|---|---|---|
| Parameter | T19 | All | Shoaling | Surf |
| $U_m$ | 0.387 | 0.001 | 0.343 | 0.134 |
| $\langle u \rangle$ | 0.126 | 0.002 | 0.01 | 0.075 |
| $\langle u^3 \rangle$ | 0.091 | 0.028 | 0.248 | 0.002 |
| $\langle u_{shortwave}{}^3 \rangle$[a] | 0.589 | 0.08 | 0.418 | 0.125 |
| $a_{spike}$ | 0.716 | 0.098 | 0.582 | 0.001 |
| $\psi$ | 0.383 | 0.003 | 0.318 | 0.145 |
| $\theta$ | 0.321 | – | 0.286 | 0.122 |
| $H/h$ | 0.896 | 0.072 | 0.663 | 0.032 |

[a]Here $f > 0.05$ Hz.

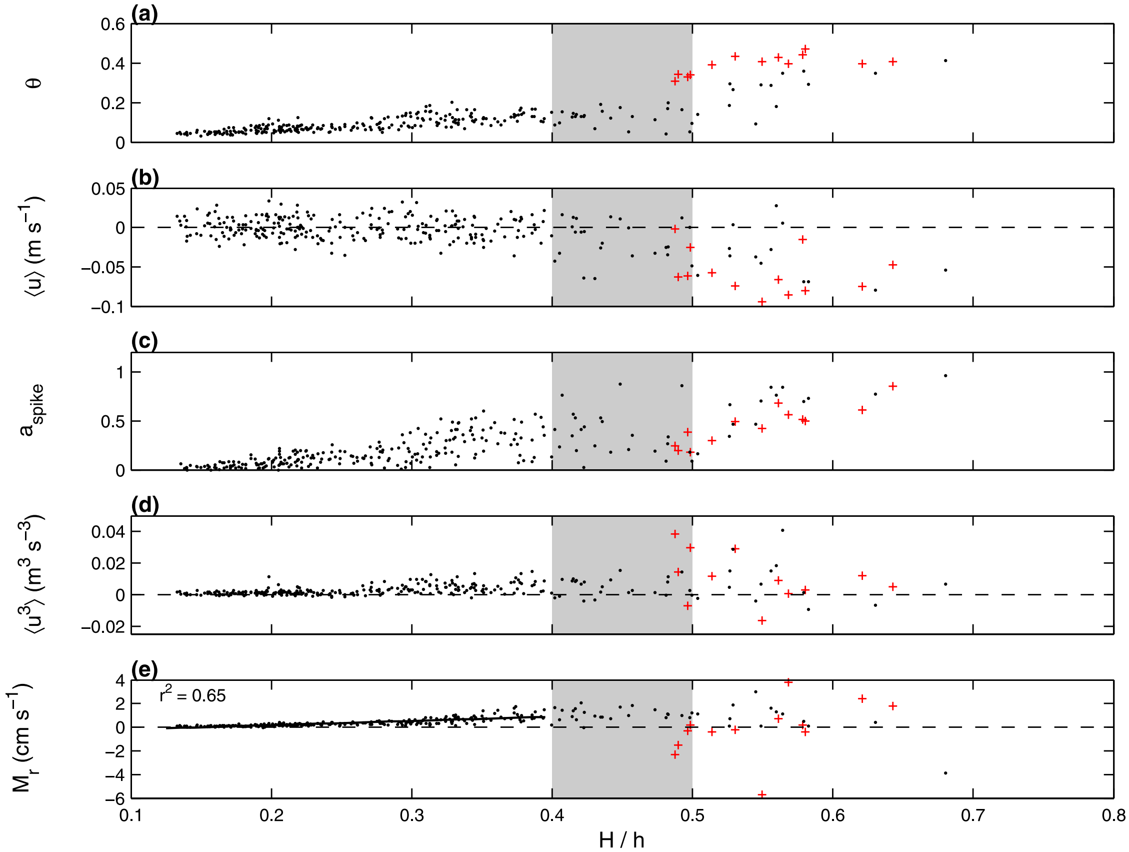


**Figure 12.** Ripple migration rate related to wave parameters. (a) Near-bed Shields parameter $\theta$; (b) mean cross-shore flow velocity measured 3 cm above the bed $\langle u \rangle$; (c) dimensional acceleration skewness $a_{spike}$; (d) velocity skewness $\langle u^3 \rangle$; and (e) ripple migration rate $M_r$. Calm ($H_s$ < 0.75 m) conditions are shown by dots, and energetic ($H_s$ > 0.75 m) conditions are shown by crosses. The shaded region represents the transition from surf to shoaling zones between $H/h$ = 0.4–0.5, encompassing data from *Plant et al.* [1999] and *Thornton and Guza* [1982].

[38] Even a casual inspection of the suspended flux data revealed that the low-energy data are fundamentally different from the high-energy data. Specifically, suspended fluxes in the surf zone are generally onshore under low waves and offshore under high waves. Such dissimilar behavior is also evident from the beach morphological response, which is characterized by mid-to-upper beach accretion and erosion under low and high waves, respectively [*Masselink et al.*, 2007]. The data are therefore divided into two main classes: (1) calm conditions with $H_s$ < 0.75 m; and (2) energetic conditions with $H_s$ > 0.75 m; this value was chosen because it separates periods of berm erosion from berm accretion [*Masselink et al.*, 2007].

[39] Using $H/h$ as an indication of cross-shore location, with the surf zone starting at $H/h$ = 0.4–0.5, Figure 14 shows the cross-shore variation in the net suspended flux and the ripple flux under low- and high-wave conditions. For the purpose of the present paper, the salient feature of Figure 14 is that over most of the nearshore zone, the ripple transport is clearly of secondary importance to the suspended fluxes; however, being approximately 30% as large as the measured suspended fluxes, it transports a significant volume of sediment. Only under shoaling waves some distance away from the surf zone are the two types of sediment fluxes comparable. Another characteristic feature is the difference between the suspended fluxes under calm and energetic conditions. Under low-wave conditions, the suspended flux is mainly onshore, both within and outside the surf zone, whereas under energetic conditions, the suspended flux is onshore around the breakpoint (and supposedly under shoaling waves) and offshore in the surf zone.

## 8. Discussion

[40] This paper discusses the geometry and dynamics of wave ripples in an environment with variable wave conditions ($H_s$ = 0.5–2 m), a macrotidal tide range (spring tide range = 5 m), shallow water depths ($h$ = 1–3 m) and relatively coarse bed material ($D_{50}$ = 0.6 mm). Such conditions have hitherto not been described in the ripple literature. At a cursory glance, "our" ripples are most comparable to those monitored by *Doucette* [2002a], who observed 10-cm-high vortex ripples just outside the surf zone on a coarse-sand beach. However, the wave conditions encountered in the latter study were much less energetic ($H_b$ < 0.2 m) and the ripple migration rates were significantly smaller (<0.2 cm min$^{-1}$). Moreover, the ripples were

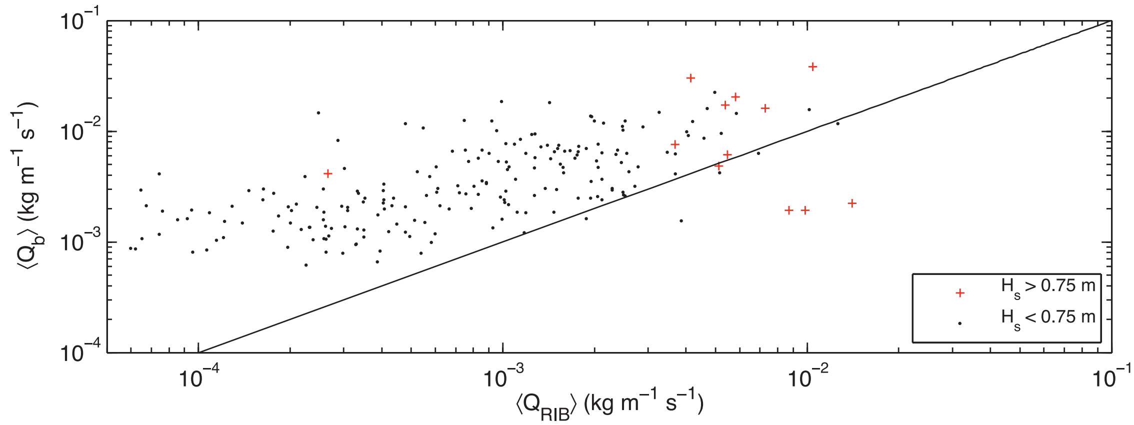


**Figure 13.** Transport rate determined from ripple migration compared to that predicted using the bed load formulation of *Ribberlink* [1998], for both calm (dot) and energetic (cross) conditions. The solid line is the 1:1 perfect fit between the data.

significantly longer ($\lambda$ = 0.5–1 m) and were orbital, rather than suborbital.

[41] Scaling parameters, such as the Mobility number $\psi$ and the Shields parameter $\theta$, allow a comparison between the present coarse-sand data set and previous recent field investigations into ripple dynamics conducted on fine-sand substrates. In addition to $\psi$ and $\theta$, another important determinant is the relative wave height $H/h$, which indicates the relative position in the nearshore zone [*Plant et al.*, 1999] and encapsulates conceptually a range of other important hydrodynamic parameters, including dissipation rate, wave nonlinearity, percentage of breaking waves, and bed return flow velocity. For the present data set, which was collected from a single location on the intertidal profile with a local gradient of *c.* 0.03, the outer surf zone is characterized by $H/h$ = 0.4–0.5, and represents the transition between the shoaling wave zone ($H/h$ < 0.4) and the saturated surf zone ($H/h$ > 0.5). Our data neatly fall into a low-wave and a high-wave data cluster, clearly demarcated by a significant wave height of 0.75 m. The low-wave ripple data were mainly collected from the shoaling wave zone and the outer breaker region ($H/h$ = 0.1–0.5), whereas the high-

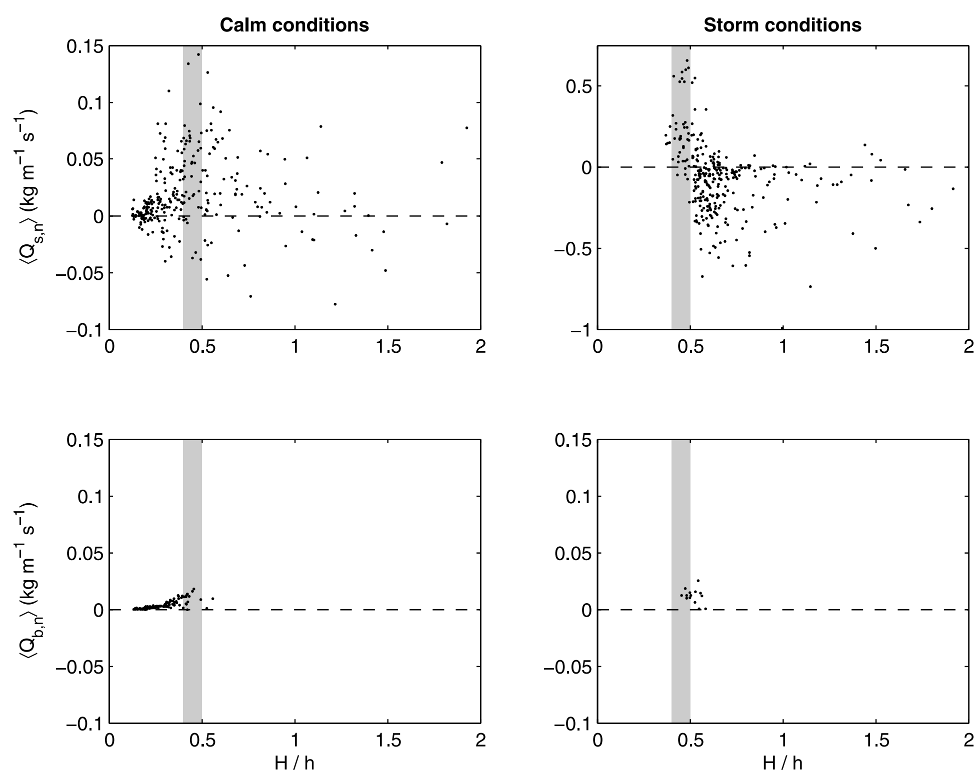


**Figure 14.** Sediment fluxes across the nearshore during calm and storm conditions. (top) Net suspended sediment flux. (bottom) Net sediment flux due to ripple migration. The region of wave breaking is indicated by the shaded area. Note the different vertical scales used in the plots for storm conditions.

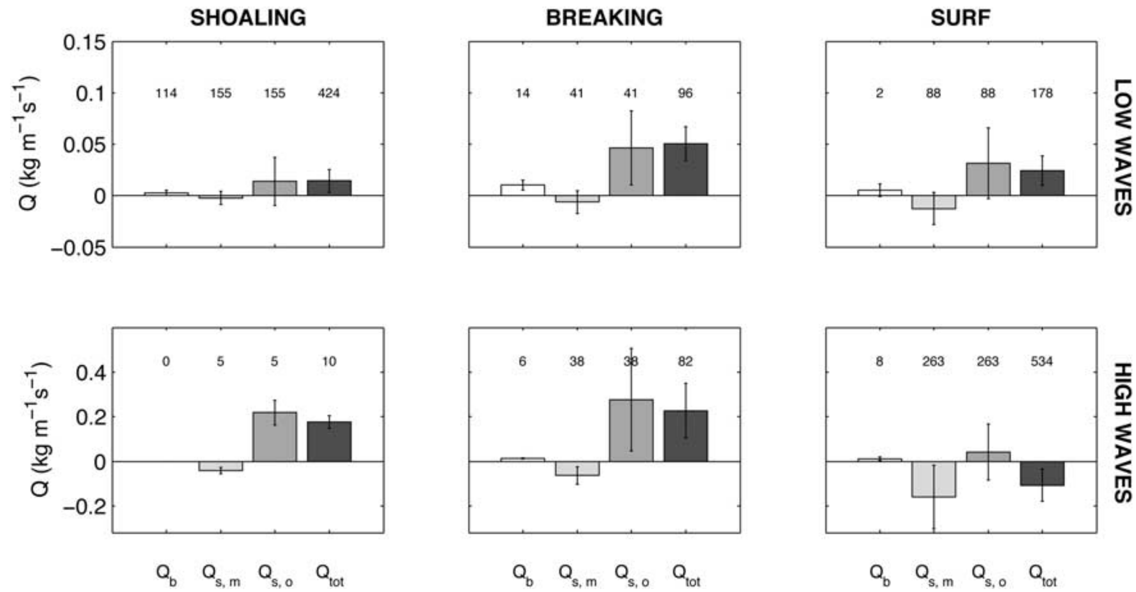


**Figure 15.** Summary of sediment transport under shoaling, breaking, and surf zone conditions for both (top) calm and (bottom) storm conditions. Bars indicate transport due to ripple migration $Q_b$ mean suspended transport $Q_{s,m}$, oscillatory suspended transport $Q_{s,o}$, and total sediment transport $Q_{tot}$. The error bars plot 1 standard deviation of the bar totals, and the values above the bars are the number of observations contained within the bar.

wave ripple data were mainly gathered from the outer surf zone and part of the saturated surf zone ($H/h$ = 0.4–0.6). Because of fundamental differences in ripple and suspended sediment dynamics, the data are best discussed by separating the low- and high-wave conditions. Figure 15 summarizes the bed form and suspended sediment fluxes under shoaling, breaking and surf conditions for both high- and low-wave conditions. During low-wave conditions, bed form and suspended fluxes are of the same order of magnitude and net transport is onshore across the entire shoreface. In contrast, during high-wave events, suspended fluxes are an order of magnitude greater than bed form transport, and in the saturated surf zone fluxes are directed offshore owing to the dominance of the mean flow component.

### 8.1. Low-Wave Conditions

[42] Linear ripples with heights of 4–6 cm and lengths of 25–40 cm are present over most of the nearshore zone when subjected to low-wave conditions. Seaward of the surf zone, bed shear stresses are characterized by $\psi$ < 20 and $\theta$ < 0.1. Such stresses are similar to those encountered in water depths in excess of 10 m over fine-sand substrates described by, for example, *Boyd et al.* [1988], *Amos et al.* [1999] and *Traykovski et al.* [1999]. In common with these studies, the ripples have a steepness of c. 0.15 and are vortex ripples; however, the coarse-sand ripples in shallow water are classified as suborbital, whereas the fine-sand ripples in deep water are generally orbital.

[43] The bed shear stresses progressively increase during wave shoaling and $\psi$ and $\theta$ attain values of 20–40 and 0.1–0.2, respectively, in the outer surf zone. Despite these larger stresses, the scale and shape of the ripples do not change significantly. The presence of vortex ripples in the outer surf zone of sandy beaches is unusual; one would expect postvortex ripples, plane bed conditions or large three-dimensional bed forms to prevail [e.g., *Hay and Bowen*, 1993; *Osborne and Vincent*, 1993; *Crawford and Hay*, 2001; *Hanes et al.*, 2001; *Saulter et al.*, 2003]. The transformation from vortex to postvortex ripples occurs in the "break-off region" of *Grant and Madsen* [1982] and commences at approximately $\psi$ > 50 and $\theta$ > 0.2 [*Nielsen*, 1981]. Owing to the coarseness of the sediment, such values are not attained under moderate breaking wave action, even with wave orbital velocities exceeding 0.8 m s$^{-1}$. The large ripple steepness values are predicted well by the equations of *Nielsen* [1981] and *Wiberg and Harris* [1994]. Vortex ripples are also expected to be present in the saturated surf zone, because bed shear stresses in this region are comparable to those found in the outer surf zone. Unfortunately, the SRP did not yield reliable data from the saturated surf zone owing to insufficient water depth, but visual observations confirm that the bed morphology inside the surf zone is similar to that in the outer breaker region.

[44] Ripple migration is almost exclusively in the onshore direction and increases from 1 mm min$^{-1}$ under shoaling waves, to 1 cm min$^{-1}$ in the outer surf zone. These migration rates are comparable to those observed over fine-sand bottoms in deep water [e.g., *Traykovski et al.*, 1999] and shallow water [*Osborne and Vincent*, 1993], respectively. The ripple migration rate is significantly and positively related to $H/h$, but also scales reasonably well with higher orders of the wave motion, such as wave orbital velocity (and its derivatives) and nonlinearity (velocity asymmetry and skewness) [cf. *Vincent and Osborne*, 1993]. Because these hydrodynamic parameters covary, and all show a progressive increase in the onshore direction toward the surf zone, it is impossible to determine which one of them is the most relevant.

[45] The migration rate of the ripples reaches a maximum of 1–2 cm min$^{-1}$ around $H/h$ = 0.45 and it is unclear why

migration rates do not increase any further with increased shear stresses in the outer surf zone. *Amos et al.* [1999] found that as suspension becomes important under increasingly energetic conditions, ripple migration rates decrease with increasing bed shear stress, and interpreted this threshold as the start of the break-off region. However, this explanation is contradicted by the persistence of the vortex ripples in the outer surf zone region. An alternative, and more likely, explanation is that the onshore migration of the ripples becomes impeded by the seaward directed mean flows. Both *Hay and Bowen* [1993] and *Doucette* [2002b] found that ripples are affected even by weak mean cross-shore currents and start migrating offshore when the mean flow velocity exceeds 3–5 cm $s^{-1}$. Offshore-directed mean flow velocities in the outer surf zone are of this order and may well have resulted in a slowing down of the onshore migrating ripples.

[46] Ripple transport rates derived from the migrating bed forms increase from 0.001 kg $m^{-1}$ $s^{-1}$ under shoaling waves, to 0.01 kg $m^{-1}$ $s^{-1}$ in the outer surf zone. The *Ribberlink* [1998] bed load transport equation underpredicts the transport due to ripple migration by almost an order of magnitude. This is most likely due to the significant and positive contribution of suspended transport to ripple migration, and is similar to the findings of *Traykovski et al.* [1999], who obtained a similar result using the *Meyer-Peter and Müller* [1948] bed load formula. This contradicts the observations of *Hay and Bowen* [1993] who found good agreement between the transport rate associated with the migration of large-scale bed forms in the shallow nearshore and that predicted by the *Madsen and Grant* [1977] and [*Watanabe*, 1982] bed load transport formulae.

[47] Despite the coarse grain size ($w_s$ = 8 cm $s^{-1}$) and low average bed shear stresses, significant sediment suspension was observed throughout this study. One explanation is that only the finest size fractions are suspended [e.g., *Williams et al.*, 1996; *Thorne et al.*, 2002]; however, since there is very little fine sediment available (greater than 95% of the bed sediment has a fall velocity in excess of 5 cm $s^{-1}$), the sediment in suspension is unlikely be significantly finer than the median bed sediment. There are, however, a number of alternative reasons as to why sediment is suspended in the present study despite the relatively low-energy flow conditions. Firstly, sediment suspension is an intermittent, rather than continuous process [*Hanes*, 1988]. Sediment was found to be suspended from the bed primarily during the peak onshore phase of the flow, when bed shear stresses are considerably greater than the time-average shear stress. Moreover, it is well known [*Nielsen*, 1992] that bed stresses are enhanced near ripple crests, especially when the ripples are characterized by a large steepness. Finally, strong flow accelerations under the onshore phase of highly asymmetric waves also have a significant and positive effect on bed shear stresses, thereby enhancing suspension [*Nielsen*, 2006].

[48] The dominant timescale associated with the suspension process, both inside and outside the surfzone, is the incident-wave timescale. Diver observations suggest that sediment is suspended mainly during the onshore stroke of the incident wave; is transported onshore over several ripple wave lengths; and settles to the bed prior to flow reversal. These qualitative observations are strongly supported by the data, especially the cospectra between $u$ and $c$, which consistently show a pronounced onshore peak at the incident wave frequency due to the coincidence of maximum suspended sediment concentrations with the onshore stroke of the wave. It is not uncommon for net suspended fluxes over vortex ripples in fine sand to be in the offshore direction [e.g., *Davies and Thorne*, 2005]. This occurs when sediment suspended during the onshore stroke of the wave is ejected high into the water column during free-stream flow reversal, and is subsequently transported seaward during the offshore stroke of the wave. However, the relatively large size of the bed material in the present study enables the sediment entrained during the onshore stroke of the wave to settle to the bed prior to flow reversal, thus undergoing net onshore transport.

[49] The preferential sediment resuspension during the onshore stroke of the wave indicates that bed shear stresses under wave crests are larger than under wave troughs, and, at least, three mechanisms are available to explain this asymmetry: (1) wave-induced boundary ventilation resulting from infiltration under the wave crest and exfiltration under the wave trough [*Conley and Inman*, 1992]; (2) positive wave skewness characterized by stronger onshore than offshore velocities [*Osborne and Greenwood*, 1992a, 1992b]; and/or (3) strong flow acceleration during the onshore stroke of the wave due to vertical wave asymmetry (crest asymmetry) [*Hanes and Huntley*, 1986; *Hoefel and Elgar*, 2003]. An evaluation of these explanations is beyond the scope of the present paper, but it is worth pointing out that the wave skewness $\langle u^3 \rangle$ for most of the data is close to zero, whereas the wave asymmetry $a_{spike}$ is significantly larger than zero.

[50] The net, vertically integrated suspended sediment flux is highly variable, but predominantly in the onshore direction. The variability in the suspended fluxes is not only due to the stochastic nature of the sediment suspension process, but also reflects the differing locations of the suspended sediment measurements in relation to the ripple morphology: the suspended sediment flux rate (and direction) may vary greatly depending on whether data are collected above the ripple crest or the ripple trough [*Davies and Thorne*, 2005]. Net suspended sediment fluxes under shoaling waves are of the same order as the ripple transport rates, but suspended fluxes in the outer surf zone are at least 1 order of magnitude greater than the bed form transport rates. The total sediment flux (ripple plus suspended transport) peaks in the outer surf zone and decreases over most of the saturated surf zone (Figure 15). The morphological response that such a sediment transport distribution would induce is the formation of a bar feature seaward of the outer surf zone, at $H/h$ = 0.5–0.6. Such a bar did indeed form over an extended period of low waves encountered during the field campaign [*Masselink et al.*, 2007].

## 8.2. High-Wave Conditions

[51] Only limited ripple data were collected under energetic wave conditions: the instrument rig was deployed too high on the beach to record large shoaling waves and the surf zone conditions were mostly too energetic for the SRP to reliably record bed levels owing to the presence of bubbles in the water. However, several glimpses of the

bed were obtained under these conditions, sufficient to warrant a brief discussion.

[52] In the outer surf zone, conditions are characterized by $\psi > 50$ and $\theta > 0.2$, indicative of the start of the break-off region. The limited data available suggest that the vortex ripples are replaced by ripples with a similar height (0.05 m), but a longer wave length (>0.5 m), and therefore smaller ripple steepness (<0.1), perhaps similar to the large wave ripples observed by *Hanes et al.* [2001], *Gallagher* [2003] and *Ngusaru and Hay* [2004]. Under the most energetic conditions, no reliable ripple data are available from the SRP, but measurements of the depth of disturbance suggest that maximum ripple heights of 0.1–0.25 m are typical under such conditions [*Masselink et al.*, 2007].

[53] The longer and less steep ripples migrate onshore, as well as offshore, possibly in relation to significant mean cross-shore flows. Correlations between ripple migration rate and velocity flow parameters (e.g., wave orbital velocity and skewness) do not yield any significant relationships, but there are not sufficient data available to explore these relationship in any great depth. What is clear, however, is that the bed form transport rates are several orders of magnitude less than the suspended fluxes (Figure 15). In the outer surf zone, the net suspended flux is onshore and attributable to the oscillatory flux component; in the saturated surf zone, the net flux is offshore and due to the mean flux component driven by the offshore-directed flow. Theoretically, such a sediment transport pattern would result in deposition at the seaward margin of the saturated surf zone ($H/h = 0.5$), and conform to the breakpoint hypothesis of bar formation [*Dhyr-Nielsen and Sorensen*, 1970; *Roelvink and Stive*, 1989].

## 9. Conclusions

[54] Suborbital vortex ripples with $\eta$ = 5 cm and $\lambda$ = 35 cm were observed in the nearshore of a macrotidal coarse sand beach during a range of wave conditions. Despite increasing bed shear stresses during wave shoaling and breaking, the shape and scale of the ripples did not change significantly. Owing to the coarseness of the sediment, there was no transition from vortex to postvortex ripples because the ‘‘break-off’’ region [*Grant and Madsen*, 1982] was never reached. Empirical models, such as those of *Nielsen* [1992] and *Wiberg and Harris* [1994], competently predict the ripple steepness, but cannot successfully estimate $\eta$ and $\lambda$.

[55] Ripple migration rates across the nearshore depend on their location relative to the breakpoint and cannot simply be related to the energy level of the hydrodynamic forcing. During low-wave conditions, $M_r$ is in the onshore direction at rates of 0.1 cm min$^{-1}$ under shoaling waves, and up to 2 cm min$^{-1}$ in the outer surf zone. $M_r$ is significantly correlated with $H/h$, but also scales reasonably well with higher orders of wave motion, such as orbital velocity, and nonlinearity; however, since these parameters covary and progressively increase toward the surf zone, it is impossible to determine which is most relevant. Maximum migration rates are located in the outer surf zone, and do not increase any further with increased shear stresses moving landward. The persistence of vortex ripples in the outer surf zone suggests that it is the seaward directed mean flow, which impedes the landward migration of the ripples, rather than the start of the break-off region where ripples become postvortex as suspension increases.

[56] Ripple transport rates derived from bed form migration in the shoaling wave zone are underpredicted by the bed load equation of *Ribberlink* [1998], strongly suggesting that suspended load transport also contributes significantly, if not dominantly, to ripple migration. Under low-wave conditions, net suspended sediment fluxes under shoaling waves are of the same order of magnitude as the bed form rates, but in the outer surf zone they are at least one order of magnitude greater than the bed form rates. The total sediment flux peaks in the outer surf zone and decreases through the saturated surf zone, conductive to bar formation seaward of the outer surf zone. Under high-wave conditions, ripple transport rates are several orders of magnitude less than the suspended fluxes. In the outer surf zone the net flux is onshore and attributable to the oscillatory flux component, and in the saturated surf zone, the net flux is offshore and due to the mean flux component driven by the offshore-directed mean flow.

[57] Suspension processes, both inside and outside the surf zone, are predominantly at the incident-wave timescale. A pronounced onshore flux-coupling exists owing to the coincidence of maximum suspended sediment concentrations with the onshore stroke of the wave. The relatively coarse grain size of the bed material enables the sediment entrained during the onshore stroke of the wave to settle to the bed prior to flow reversal. The net suspended transport is thus onshore, in contrast to previous observations of net offshore suspended fluxes over vortex ripples in fine sands.

[58] **Acknowledgments.** We would like to thank Peter Ganderton, Tony Butt, Jon Tinker, Daniel Buscombe, Tamsin Watt, Louise Hockley, and Nigel Auger for invaluable assistance in the field. Many thanks go to Nicholas King and the King family for letting us use their holiday home as our field station. This research was funded by NERC grant NER/A/S/2003/00553 (Cross-shore sediment transport and profile evolution on natural beaches—the X-Shore project) awarded to P. R., G. M., and T. O. H.

## References

Allen, J. R. L. (1970), A quantitative model of climbing ripples and their cross-laminated deposits, *Sedimentology*, *14*, 5–26.

Amos, C. L., A. J. Bowen, D. A. Huntley, J. T. Judge, and M. Z. Li (1999), Ripple migration and sand transport under quasi-orthogonal combined flows on the scotian shelf, *J. Coastal Res.*, *15*, 1–14.

Austin, M. J., and G. Masselink (2007), The effect of bedform dynamics on computing suspended sediment flux using obtical backscatter sensors and current meters, *Coastal Eng.*, in press.

Bagnold, R. A. (1963), Beach and neashore processes, in *The Sea*, edited by M. N. Hill, pp. 507–553, Wiley-Interscience, New York.

Boyd, R., D. L. Forbes, and D. E. Heffler (1988), Time-sequence observations of wave-formed sand ripples on an ocean shoreface, *Sedimentology*, *35*, 449–464.

Butt, T., J. R. Miles, P. Ganderton, and P. E. Russell (2002), A simple method for calibrating optical backscatter sensors in high concentrations of non-cohesive sediments, *Mar. Geol.*, *192*, 419–424.

Clifton, H. E. (1976), Wave-formed sedimentary structures: A conceptual model, *SEPM Spec. Publ.*, *24*, 126–148.

Clifton, H. E., and J. R. Dingler (1984), Wave-formed structures and paleoenvironmental reconstruction, *Mar. Geol.*, *60*, 165–198.

Conley, D. C., and D. L. Inman (1992), Field observations of the fluid-granular boundary layer under near-breaking waves, *J. Geophys. Res.*, *97*, 9631–9643.

Crawford, A. M., and A. E. Hay (2001), Linear transition ripple migration and wave orbital velocity skewness: Observations, *J. Geophys. Res.*, *106*, 14,113–14,128.

Crawford, A. M., and A. E. Hay (2003), Wave orbital velocity skewness and linear transition ripple migration: Comparison with weakly nonlinear theory, *J. Geophys. Res.*, *108*(C3), 3091, doi:10.1029/2001JC001254.

Davidson, M. A., P. E. Russell, D. A. Huntley, and J. Hardisty (1993), Tidal asymmetry in suspended sand transport on a macrotidal intermediate beach, *Mar. Geol.*, *110*, 333–353.

Davidson, M. A., D. A. Huntley, R. A. Holman, and K. George (1998), The evaluation of large scale (km) intertidal beach morphology on a macrotidal beach using video images, paper presented at International Conference on Coastal Dynamics, Am. Soc. of Civ. Eng., Copenhagen.

Davies, A. G., and P. D. Thorne (2005), Modelling and measurement of sediment transport by waves in the vortex ripple regime, *J. Geophys. Res.*, *110*, C05017, doi:10.1029/2004JC002468.

Dhyr-Nielsen, M., and T. Sorensen (1970), Sand transport phenomena on coasts with bars, paper presented at 12th International Conference on Coastal Engineering, Am. Soc. of Civ. Eng., Washington, D. C.

Dingler, J. R. (1974), Wave-formed ripples in nearshore sands, Ph.D. thesis, Univ. of Calif., San Diego.

Doucette, J. S. (2002a), Geometry and grain-size sorting of ripples on low-energy sandy beaches: Field observations and model predictions, *Sedimentology*, *49*, 483–503.

Doucette, J. S. (2002b), Bedform migration and sediment dynamics in the nearshore of a low-energy sandy beach in southwestern Australia, *J. Coastal Res.*, *18*, 576–591.

Dyer, K. R., and R. L. Soulsby (1988), Sand transport on the continental-shelf, *Annu. Rev. Fluid Mech.*, *20*, 295–324.

Fredsoe, J., and R. Deigaard (1992), *Mechanics of Coastal Sediment Transport*, World Sci., Hackensack, N. J.

Gallagher, E. L. (2003), A note on megaripples in the surf zone: Evidence for their relation to steady flow dunes, *Mar. Geol.*, *193*, 171–176.

Grant, W. D., and O. S. Madsen (1982), Movable bed roughness in unsteady oscillatory flow, *J. Geophys. Res.*, *87*, 469–481.

Grant, W. D., and O. S. Madsen (1986), The continental-shelf bottom boundary-layer, *Annu. Rev. Fluid Mech.*, *18*, 265–305.

Hanes, D. M. (1988), Intermittent sediment suspension and its implications to sand tracer dispersal in wave-dominated environments, *Mar. Geol.*, *81*, 175–183.

Hanes, D. M., and D. A. Huntley (1986), Continuous measurements of suspended sand concentration in a wave dominated nearshore environment, *Cont. Shelf Res.*, *6*, 585–596.

Hanes, D. M., V. Alymov, Y. S. Chang, and C. Jette (2001), Wave-formed sand ripples at Duck, North Carolina, *J. Geophys. Res.*, *106*, 22,575–22,592.

Hay, A. E., and A. J. Bowen (1993), Spatially correlated depth changes in the nearshore zone during autumn storms, *J. Geophys. Res.*, *98*, 12,387–12,404.

Hay, A. E., and T. Mudge (2005), Principal bed states during SandyDuck97: Occurrence, spectral anisotropy, and the bed state storm cycle, *J. Geophys. Res.*, *110*, C03013, doi:10.1029/2004JC002451.

Hoefel, F., and S. Elgar (2003), Wave-induced sediment transport and sandbar migration, *Science*, *299*, 1885–1887.

Huntley, D. A., and D. M. Hanes (1987), Direct measurement of suspended sediment transport, paper presented at Coastal Sediments '87, Am. Soc. of Civ. Eng., New Orleans, La.

Huntley, D. A., C. L. Amos, J. J. Williams, and J. D. Humphrey (1991), Estimating bedload transport on continental shelves by observations of ripple migration—An assessment, in *Euromech 262—Sand Transport in Rivers, Estuaries and the Sea*, edited by R. Soulsby and R. Betess, pp. 17–24, A. A. Balkema, Rotterdam.

Jaffe, B. E., R. W. Sternberg, and A. H. Sallenger (1984), The role of suspended sediment in shore-normal beach profile changes, paper presented at 19th International Conference on Coastal Engineering, Am. Soc. of Civ. Eng., Houston, Tex.

Madsen, O. S., and W. D. Grant (1977), 1977, paper presented at 15th International Coastal Engineering Conference, Am. Soc. of Civ. Eng., New York.

Malarkey, J., and A. G. Davies (2003), A non-iterative proceedure for the Wiberg and Harris [1994] oscillatory sand ripple predictor, *J. Coastal Res.*, *19*, 738–739.

Masselink, G., and C. Pattiaratchi (2000), Tidal asymmetry in sediment resuspension on a macrotidal beach in northwestern Australia, *Mar. Geol.*, *163*, 257–274.

Masselink, G., and A. D. Short (1993), The effect of tide range on beach morphodynamics and morphology: A conceptual beach model, *J. Coastal Res.*, *9*, 785–800.

Masselink, G., N. Auger, P. E. Russell, and T. O'Hare (2007), Short-term morphological change and sediment dynamics in the intertidal zone of a macrotidal beach, *Sedimentology*, *54*, 39–53.

Meyer-Peter, E., and R. Müller (1948), Formulas for bed-load transport, in *Report on the 2nd Meeting of the International Association for Hydraulic Structures Research*, vol. 2, pp. 39–64, Int. Assoc. for Hydraul. Struct. Res., Stockholm.

Miller, M. C., and P. D. Komar (1980), A field investigation of the relationship between oscillation ripple spacing and the near-bottom water orbital motions, *J. Sediment. Petrol.*, *50*, 183–191.

Ngusaru, A. S., and A. E. Hay (2004), Cross-shore migration of lunate megaripples during Duck94, *J. Geophys. Res.*, *109*, C02006, doi:10.1029/2002JC001532.

Nielsen, P. (1981), Dynamics and geometry of wave-generated ripples, *J. Geophys. Res.*, *86*, 6467–6472.

Nielsen, P. (1992), *Coastal Bottom Boundary Layers and Sediment Transport*, World Sci., Hacksensack, N. J.

Nielsen, P. (2006), Sheet flow sediment transport under waves with acceleration skewness and boundary layer streaming, *Coastal Eng.*, *53*, 749–758.

Osborne, P. D., and B. Greenwood (1992a), Frequency dependent cross-shore suspended sediment transport 1. A non-barred shoreface, *Mar. Geol.*, *106*, 1–24.

Osborne, P. D., and B. Greenwood (1992b), Frequency dependent cross-shore suspended sediment transport 2. A barred shoreface, *Mar. Geol.*, *106*, 25–51.

Osborne, P. D., and C. E. Vincent (1993), Dynamics of large and small-scale bedforms on a macrotidal shoreface under shoaling and breaking waves, *Mar. Geol.*, *115*, 207–226.

Plant, N. G., R. A. Holman, M. H. Freilich, and W. A. Birkermeir (1999), A simple model for interannual sandbar behaviour, *J. Geophys. Res.*, *104*, 15,755–15,776.

Plant, N. G., B. G. Ruessink, and K. M. Wijnberg (2001), Morphologic properties derived from a simple cross-shore sediment transport model, *J. Geophys. Res.*, *106*, 945–958.

Ribberlink, J. S. (1998), Bed-load transport for steady flows and unsteady oscillatory flows, *Coastal Eng.*, *34*, 59–82.

Roelvink, J. A., and M. J. F. Stive (1989), Bar-generating cross-shore flow mechanisms on a beach, *J. Geophys. Res.*, *94*, 4785–4800.

Ruessink, B. G., K. T. Houwman, and P. Hoekstra (1998), The systematic contribution of transporting mechanisms to the cross-shore sediment transport in water depths of 3 to 9 m, *Mar. Geol.*, *152*, 295–324.

Saulter, A. N., P. E. Russell, E. L. Gallagher, and J. R. Miles (2003), Observations of bed level changes in a saturated surf zone, *J. Geophys. Res.*, *108*(C4), 3112, doi:10.1029/2000JC000684.

Smith, E. R., and N. C. Kraus (1991), Laboratory study of wave-breaking over bars and artificial reefs, *J. Waterw. Port Coastal Ocean Eng.*, *117*, 307–325.

Swart, D. H. (1974), Offshore sediment transport and equilibrium beach profiles, *Laboratory Publ. 131*, Delft Hydraul., Delft, Netherlands.

Thorne, P. D., and D. M. Hanes (2002), A review of acoustic measurements of small-scale sediment processes, *Cont. Shelf Res.*, *22*, 603–632.

Thorne, P. D., J. J. Williams, and A. G. Davies (2002), Suspended sediments under waves measured in a large-scale flume facility, *J. Geophys. Res.*, *107*(C8), 3178, doi:10.1029/2001JC000988.

Thornton, E. B., and R. T. Guza (1982), Energy saturation and phase speeds measured on a natural beach, *J. Geophys. Res.*, *87*, 9400–9508.

Thornton, E. B., J. L. Swayne, and J. R. Dingler (1998), Small-scale morphology across the surf zone, *Mar. Geol.*, *145*, 173–196.

Traykovski, P., A. E. Hay, J. D. Irish, and J. F. Lynch (1999), Geometry, migration, and evolution of wave orbital ripples at LEO-15, *J. Geophys. Res.*, *104*, 1505–1524.

Vincent, C. E., and P. D. Osborne (1993), Bedform dimensions and migration rates under shoaling and breaking waves, *Cont. Shelf Res.*, *13*, 1267–1280.

Vincent, C. E., D. M. Hanes, and A. J. Bowen (1991), Acoustic measurements of suspended sand on the shoreface and the control of concentration by bed roughness, *Mar. Geol.*, *96*, 1–18.

Watanabe, A. (1982), Numerical models of nearshore currents and beach deformation, *Coastal Eng. Jpn.*, *27*, 147–161.

Wiberg, P. L., and C. K. Harris (1994), Ripple geometry in wave-dominated environments, *J. Geophys. Res.*, *99*, 775–789.

Williams, J. J., C. P. Rose, P. D. Thorne, L. E. Coates, J. R. West, P. J. Harcastle, J. D. Humphrey, S. P. Moores, and D. J. Wilson (1996), Observed suspended sediments in storm conditions, paper presented at 25th International Conference on Coastal Engineering, Am. Soc. of Civ. Eng., Orlando, Fla.

Williams, J. J., P. S. Bell, P. D. Thorne, N. Metje, and L. E. Coates (2004), Measurement and prediction of wave-generated suborbital ripples, *J. Geophys. Res.*, *109*, C02004, doi:10.1029/2003JC001882.



M. J. Austin, T. J. O'Hare, and P. E. Russell, School of Earth, Ocean and Environmental Sciences, University of Plymouth, Drake Circus, Plymouth, Devon PL4 8AA, UK. (martin.austin@plymouth.ac.uk; tohare@plymouth.ac.uk; p.russell@plymouth.ac.uk)

G. Masselink, School of Geography, University of Plymouth, Drake Circus, Plymouth, Devon PL4 8AA, UK. (g.masselink@plymouth.ac.uk)